Chemical Engineering Journal 518 (2025) 164579

Contents lists available at ScienceDirect

Chemical Engineering Journal

journal homepage: www.elsevier.com/locate/cej

2D nonlayered titanium oxynitrides intercalated with nitrogen-doped graphene for pseudocapacitive energy storage

Xiuli Li [a,c], Rui Huo [b], Zihuan Tang [a], Yulei Ren [a], Hao Song [a,*], Paul K. Chu [d,e,f], Kaifu Huo [c,*]

[a] State Key Laboratory of Advanced Refractories, Institute of Advanced Materials and Nanotechnology, Wuhan University of Science and Technology, Wuhan 430081, China
[b] School of Materials Science and Engineering, Central South University, Changsha 410083, China
[c] Wuhan National Laboratory for Optoelectronics (WNLO), School of Optical and Electronic Information, Huazhong University of Science and Technology, Wuhan 430074, China
[d] Department of Physics, City University of Hong Kong, Kowloon, Hong Kong 999077, China
[e] Department of Materials Science and Engineering, City University of Hong Kong, Kowloon, Hong Kong 999077, China
[f] Department of Biomedical Engineering, City University of Hong Kong, Kowloon, Hong Kong 999077, China

ARTICLE INFO

Keywords:
Titanium oxynitride
Spatially confined synthesis
Volumetric capacitance
In situ spectroscopy
Pseudocapacitive storage mechanism

ABSTRACT

Nanostructured titanium oxynitride (TiN_xO_{1-x}) is a promising pseudocapacitive material due to its large pseudocapacitance and high conductivity. However, the synthesis of nonlayered two-dimensional (2D) TiN_xO_{1-x} is challenging and the pseudocapacitive energy storage mechanism of TiN_xO_{1-x} is still unclear. Herein, accordion-like 2D TiN_xO_{1-x} nanosheets intercalated with nitrogen-doped graphene (TiN_xO_{1-x}/NG) are controllably fabricated by a spatially confined thermal nitridation of 1,8-diaminooctane intercalated $H_{0.8}Ni_{0.4}Ti_{1.6}O_4{\cdot}H_2O$ nanosheets. *In situ* electrochemical characterizations and theoretical calculations reveal the pseudocapacitance originates from the Faradic reaction between H^+ and N—Ti—O species accompanied by Ti valence state change and the pseudocapacitance of TiN_xO_{1-x}/NG is determined by the N—Ti—O content instead of the N/O ratio. Compared to TiN_xO_{1-x}, the electrons transfer from sandwiched NG to TiN_xO_{1-x} enhances H^+ adsorption at N active sites of N—Ti—O within TiN_xO_{1-x}/NG, giving rise to enhanced pseudocapacitance and cycling stability. Consequently, the TiN_xO_{1-x}/NG shows a large volumetric capacitance of 739.2 F cm^{-3} (616.0 F g^{-1}) at 1 A cm^{-3} and superior cyclability with 98.5 % capacitance retention after 10,000 cycles, surpassing previously reported metal oxynitrides and nitrides. The results provide insights into the controllable synthesis of 2D nonlayered TiN_xO_{1-x} and elucidate the pseudocapacitive charge storage mechanism of metal nitrides or oxynitrides.

1. Introduction

Electrochemical supercapacitors (SCs) have been extensively investigated as promising energy storage devices due to the high-power density, quick charging-discharging rate, and long cycling lifetime [1]. Compared to traditional battery systems with high energy density [2–4], SCs have high power capability and thus could deliver energy within seconds or minutes. The performance of SCs is fundamentally determined by electrode materials, and therefore, it is vital to develop electrode materials with high capacitance and high power capability for advanced SCs. Porous carbon materials that store charge electrostatically *via* ion adsorption/desorption are widely utilized as electrode materials in electric double-layer capacitors (EDLCs) [5–7]. However, their relatively small specific capacitances restrict the applications requiring energy densities [8,9]. In contrast, transition metal oxides (TMOs) and transition metal nitrides (TMNs) that store charge *via* surface or near-surface reversible Faradic reactions exhibit large pseudocapacitance [10,11]. However, the TMOs generally have poor electrical conductivity and power capability due to the low conductivity. The TMNs such as MoN and TiN possess metallic-like high conductivity and good mechanical and chemical stability, but a smaller storage capacitance than their TMO counterparts [12,13]. The motivation for developing pseudocapacitors is to achieve both high energy and high-power densities by the same electrode material.

Recently, transition metal oxynitrides (TMONs) such as titanium oxynitrides, vanadium oxynitrides, and molybdenum oxynitrides have

* Corresponding authors.
E-mail addresses: songhao201809@wust.edu.cn (H. Song), kfhuo@hust.edu.cn (K. Huo).

https://doi.org/10.1016/j.cej.2025.164579
Received 9 January 2025; Received in revised form 19 May 2025; Accepted 5 June 2025
Available online 7 June 2025

emerged as a new family of pseudocapacitive materials with high energy density and high-power capability by combining the advantages of TMOs and TMNs [14–18]. Among them, titanium oxynitrides (TiN_xO_{1-x}) are excellent candidates on account of their superior specific capacity and high conductivity [19,20]. The substitution of an O anion with a −2 charge by an N anion with a −3 charge in TiN_xO_{1-x} can produce more metal cation valence states and oxygen vacancies. As a result, TiN_xO_{1-x} has a larger specific capacitance and higher power capability than TiN and TiO_2 [21–23]. For example, Mouchani et al. [24] have reported that TiON nanotubes have a higher areal capacitance of 35.14 mF cm^{-2} at 0.2 mA cm^{-2} than that of TiO_2 nanotubes (3.82 mF cm^{-2}) and TiN nanotubes (25 mF cm^{-2}). Yan et al. [25] have shown the large specific capacity of 187 F g^{-1} for TiON nanoparticles anchored carbon nanotubes (CNTs/TiON) at a current density of 0.5 A g^{-1}, which is twice that of CNTs/TiO_2. Nevertheless, despite recent progress, the reported TiN_xO_{1-x} electrode materials generally have unsatisfactory specific capacitance due to the small active surface area and sluggish ion diffusion rates [26,27]. Recently, two-dimensional (2D) materials, especially titanium carbides and nitrides MXene ($Ti_{n+1}X_nT_x$), have emerged as promising electrode materials for SCs arising from the abundant surface-active sites and high electrical conductivity [28,29]. Different from 2D MXene, TiN_xO_{1-x} is non-layered materials with cubic-phase structure and it is challenging to prepare ultrathin 2D TiN_xO_{1-x} nanosheets. Moreover, the intrinsic pseudocapacitive storage mechanism of TiN_xO_{1-x} is still poorly understood.

Herein, we report accordion-like 2D TiN_xO_{1-x} intercalated with nitrogen-doped graphene (TiN_xO_{1-x}/NG) as a high-performance pseudocapacitive material for SCs. The accordion-like TiN_xO_{1-x}/NG is prepared by spatially confined thermal nitriding lamellar 1,8-diaminooctane intercalated $H_{0.8}Ni_{0.4}Ti_{1.6}O_4{\cdot}H_2O$ (HNTOH/DOE), followed by acid etching of Ni. The intercalated DOE molecules between the HNTOH layers are carbonized *in situ* to form 2D NG nanosheets, while the HNTOH layer is converted into the TiN_xO_{1-x} nanosheet sandwiched with the NG nanosheets, resulting in the formation of the layer-by-layer accordion-like TiN_xO_{1-x}/NG heterostructure. Different from the widely reported semiconductor TiO_2 or N doped TiO_2 ($TiO_{2-x}N_x$), the cubic TiN_xO_{1-x} and TiN have metallic conductivity, which allow for rapid electron transport [21–25]. Moreover, layer-by-layer TiN_xO_{1-x}/NG heterostructure enables enriched active sites and decreased diffusion distances, thereby giving rise to large specific pseudocapacitance and fast rate capability. As a result, the as-synthesized accordion-like TiN_xO_{1-x}/NG has a large volume capacity of 739.2 F cm^{-3} (616.0 F g^{-1}) at a current density of 1 A cm^{-3}, as well as superior cyclability with capacity retention of 98.5 % after 10,000 cycles in the 0.5 M H_2SO_4 electrolyte, surpassing recently reported Ti-based nitrides and oxynitrides (Table S1). Electrochemical quartz crystal microbalance (EQCM), *in situ* Raman scattering, *in situ* infrared spectroscopy, *ex situ* X-ray photoelectron spectroscopy (XPS) combined with theoretical calculations reveal that the pseudocapacitance of TiN_xO_{1-x} in H_2SO_4 originates from the Faradic reaction between H^+ and N active sites of N—Ti—O species accompanied by the reversible Ti valence state change. The previous reports reveal that the specific capacitance of metal oxynitrides or nitrides increases with the N/O ratio [30,31], however, our results confirm that the pseudocapacitance of TiN_xO_{1-x} coincides with their N—Ti—O content rather than N/O ratio and the TiN_xO_{1-x} with the higher N—Ti—O content has the largest pseudocapacitance. Density functional theory (DFT) calculations and XPS results reveal that the electron transfer from the NG to TiN_xO_{1-x} nanosheets further enhances H^+ adsorption at N—Ti—O, resulting in enhanced pseudocapacitance and cycling stability of TiN_xO_{1-x}/NG. The symmetrical all-solid-state flexible SC composed of the TiN_xO_{1-x}/NG electrodes and H_2SO_4/PVA gel-like electrolyte shows an energy density of 47.6 mWh cm^{-3} (39.8 Wh kg^{-1}) and a power density of 500.0 mW cm^{-3} (416.7 W kg^{-1}), suggesting large potential in electrochemical energy storage. This work provides insights into the design of 2D nonlayered TiN_xO_{1-x} and a better understanding of the pseudocapacitive charge storage mechanism of TiN_xO_{1-x}/NG.

2. Results and discussion

The preparation of accordion-like TiN_xO_{1-x}/NG hybrid nanosheets is illustrated schematically in Fig. 1a. The synthesis procedures for $K_{0.8}Ni_{0.4}Ti_{1.6}O_4$ (KNTO), $H_{0.8}Ni_{0.4}Ti_{1.6}O_4{\cdot}H_2O$ (HNTOH) and the HNTOH/DOE are similar to those described in previous reports [32–35]. The as-synthesized KNTO precursor (Fig. 1b and Fig. S1a) has an average size of 10 μm and the X-ray diffraction (XRD) patterns in Fig. S1b show the typical (*0k0*) diffraction pattern of a layered structure in agreement with the $K_{0.8}Ni_{0.4}Ti_{1.6}O_4$ phase [33]. The K ions between $[Ni_{0.4}Ti_{1.6}O_4]^{0.8-}$ layers are easily exchanged by hydrogen ions in diluted HNO_3 (1.0 M) to form protonated HNTOH. The scanning electron microscopy (SEM) image in Fig. 1c and XRD pattern in Fig. S1b reveals that HNTOH inherits the multilayer stacked structure of KNTO. However, the interlayer distance of HNTOH is expanded to 0.88 nm from the 0.76 nm of KNTO because the H_3O^+ has the larger ionic radius compared to K^+ [34]. After DOE molecules with larger size intercalated into HNTOH layers to form HNTOH/DOE, the d_{020} lattice spacing increases from 0.88 nm of pristine HNTOH to 1.57 nm of HNTOH/DOE (Fig. S1c). This substantial expansion of interlayer distance is attributed to the oriented arrangement of larger DOE molecules between $[Ni_{0.4}Ti_{1.6}O_4]^{0.8-}$ layers. The SEM image of HNTOH/DOE (Fig. 1d) discloses a looser layered structure compared with HNTOH, indicating that DOE molecules successfully inserted into the interlayer of HNTO. The 2D heterostructure TiN_xO_{1-x}/NG is produced by thermal nitriding of accordion-like HNTOH/DOE multilayered nanosheets at 750 °C under NH_3, followed by removal of Ni in diluted HCl. During thermal nitridation, the intercalated DOE molecules are carbonized *in situ* into the NG layer by confining carbonization [36], while the sandwiched HNTOH layers are converted into 2D TiN_xO_{1-x} decorated with metallic Ni species through phase separation. The SEM images in Fig. 1e and Fig. S1d show that Ni-TiN_xO_{1-x}/NG has a similar morphology as the HNTOH/DOE precursor except for decorated Ni nanoparticles on the nanosheets. The Ni nanoparticles anchored on the TiN_xO_{1-x} nanosheet surface could be removed with diluted HCl to produce accordion-like TiN_xO_{1-x}/NG (Fig. 1f and Fig. S1e). The XRD patterns of TiN_xO_{1-x}/NG in Fig. S1f show that all the diffraction peaks are ascribed to the cubic TiN_xO_{1-x} or TiN (PDF# 38−1420) and the Ni diffraction peak disappears. The Fourier transform infrared spectroscopy (FTIR) spectrum is employed to investigate the polymerization and carbonization of the DOE during the thermal nitridation process. The HNTOH/DOE exhibits bands of the C—N stretching (1100–1300 cm^{-1}), C—H bending (1390 cm^{-1}), and N—H bending (1480 and 1590 cm^{-1}) of DOE (Fig. S2), indicating intercalation of DOE between the HNTOH layers. After the thermal nitriding, the characteristic peaks of C—H bending and N—H bending in TiN_xO_{1-x}/NG disappear, while the peaks of C—N stretching become broadening, suggesting the DOE molecular layer is pyrolyzed into NG *via* thermal carbonization. Raman peaks at 1356, 1590 and 2847 cm^{-1} associated with the D, G, and 2D bands of NG (Fig. S3) [37,38], further indicating the DOE molecular layer is converted into NG.

To study the evolution of chemical states and N/O ratio in TiN_xO_{1-x} during thermal nitriding, four samples with different N/O ratios are prepared by varying the nitriding time (1, 3, 5, and 7 h), and the samples are denoted as N-TiO_2/NG, TiN_xO_{1-x}/NG-3, TiN_xO_{1-x}/NG-5, and TiN_xO_{1-x}/NG-7, respectively. Fig. 2a schematically illustrates the conversion procedures from titanate hydrate to TiN_xO_{1-x} by thermal nitriding under NH_3 at 750 °C. During nitridation, O anions are gradually substituted by N anions, and tetragonal-phase TiO_2 is gradually transformed into N-TiO_2 and cubic-phase TiN_xO_{1-x} [39–41]. The XRD patterns of N-TiO_2/NG, TiN_xO_{1-x}/NG-3, TiN_xO_{1-x}/NG-5, and TiN_xO_{1-x}/NG-7 are depicted in Fig. 2b. The XRD pattern of N-TiO_2/NG corresponds to tetragonal N-doped TiO_2 with a small amount of O substituted by N [42]. However, when the nitridation time goes up to 3 h, XRD pattern reveals that the tetragonal N-doped TiO_2 phase disappears, and the strong peaks at

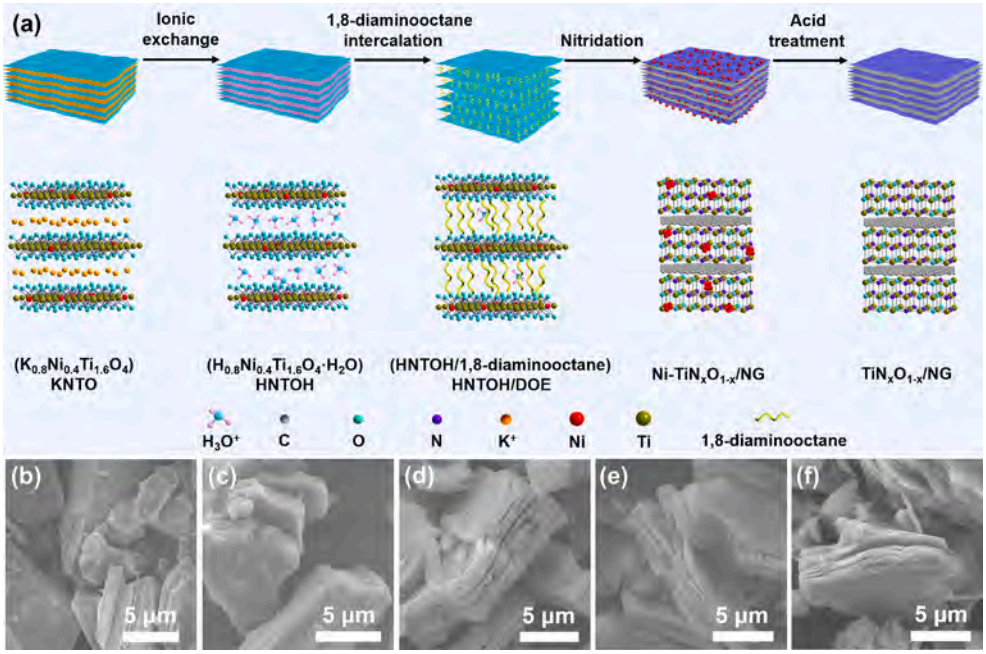

Fig. 1. Schematical illustration and SEM images of samples from KNTO to TiN_xO_{1-x}/NG nanosheets. (a) Schematical illustration of the synthesis procedures; SEM images of (b) KNTO, (c) HNTOH, (d) HNTOH/DOE, (e) Ni-TiN_xO_{1-x}/NG, and (f) TiN_xO_{1-x}/NG.

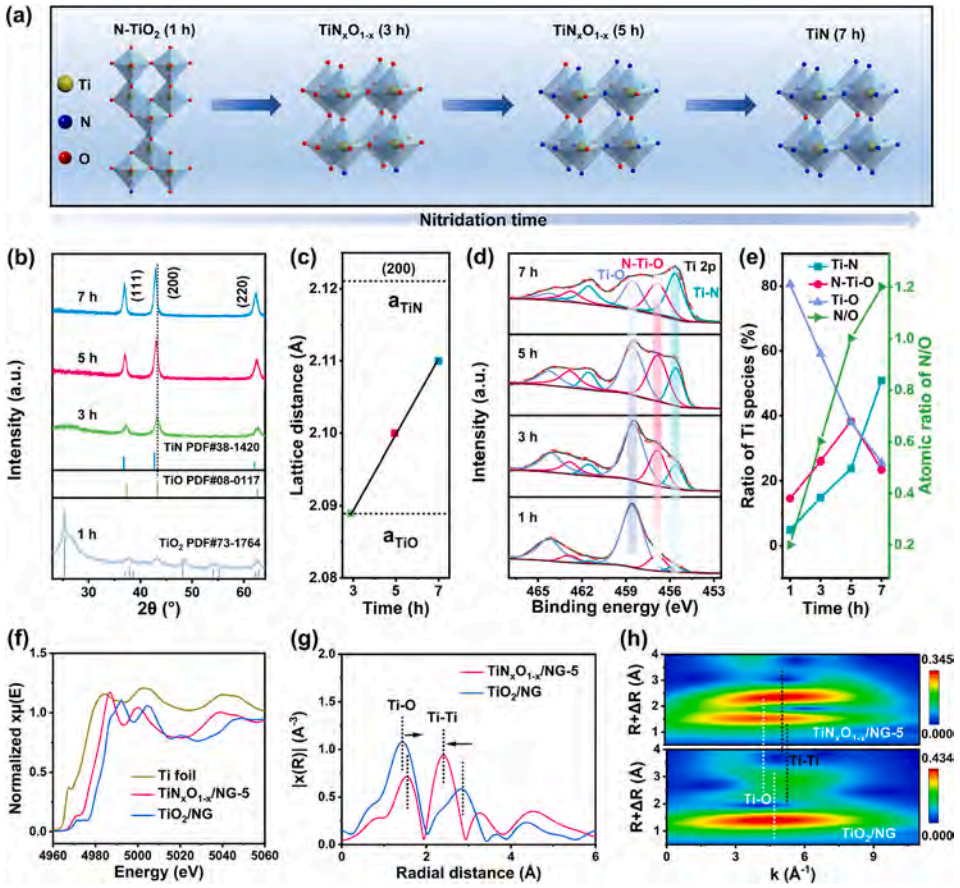

Fig. 2. The evolutions of crystal structure and composition of the as-synthesized N-TiO_2/NG, TiN_xO_{1-x}/NG-3, TiN_xO_{1-x}/NG-5, and TiN_xO_{1-x}/NG-7. (a) Schematical illustration of the crystal structure evolutions from N-TiO_2 to TiN_xO_{1-x} and TiN *via* thermal nitridation; (b) XRD patterns of N-TiO_2/NG, TiN_xO_{1-x}/NG-3, TiN_xO_{1-x}/NG-5, and TiN_xO_{1-x}/NG-7; (c) Crystal lattice distances of TiN_xO_{1-x}/NG-3, TiN_xO_{1-x}/NG-5, and TiN_xO_{1-x}/NG-7; (d) Ti 2*p* XPS spectra and (e) ratios of different Ti species and atomic ratios of N/O in N-TiO_2/NG, TiN_xO_{1-x}/NG-3, TiN_xO_{1-x}/NG-5, and TiN_xO_{1-x}/NG-7; (f) Ti K-edge XANES of Ti foil, TiN_xO_{1-x}/NG-5, and TiO_2/NG; (g) Fourier transform EXAFS spectra and (h) wavelet transform (WT) of TiN_xO_{1-x}/NG-5 and TiO_2/NG.

37.3°, 43.4°, and 62.8° are ascribed to cubic TiN_xO_{1-x} or TiO (PDF# 08−0117). As the nitriding time increases further, the diffraction peaks of TiN_xO_{1-x} gradually shift to smaller 2θ and become comparable to those of cubic TiN (PDF# 38−1420), suggesting the complete transformation into cubic TiN. The lattice distances of TiN_xO_{1-x}/NG-3, TiN_xO_{1-x}/NG-5, and TiN_xO_{1-x}/NG-7 increase with nitridation time due to more substitution of O (66 pm) by N with a larger atomic radius of 70 pm (Fig. 2c and Fig. S4). The calculated TiN_xO_{1-x} lattice distances of TiN_xO_{1-x}/NG-3, TiN_xO_{1-x}/NG-5, and TiN_xO_{1-x}/NG-7 are 2.089, 2.100, and 2.110 Å, which are within the theoretical lattice distances of cubic TiO (2.089 Å) and cubic TiN (2.121 Å), suggesting the formation of a solid solution of cubic TiN and TiO and thus the samples are best described as TiN_xO_{1-x}. The SEM images in Fig. S5 show that N-TiO_2/NG, TiN_xO_{1-x}/NG-3, TiN_xO_{1-x}/NG-5, and TiN_xO_{1-x}/NG-7 have a similar morphology, indicating topochemical conversion from HNTOH/DOE precursor to accordion-like TiN_xO_{1-x}/NG nanosheets.

The XPS survey spectrum of TiN_xO_{1-x}/NG (Fig. S6a) shows the presence of Ti, O, N, and C, and the N concentration increases with the nitriding time (Table S2). The Ti 2*p* peak in Fig. 2d can be deconvoluted into three spin-orbit doublets (for Ti 2*p*3/2 and Ti 2*p*1/2), corresponding to Ti—N (455.5, 461.5 eV), N—Ti—O (456.9, 462.9 eV) and Ti—O (458.5, 464.2 eV), respectively [43,44]. The N 1*s* spectra (Fig. S6b) further corroborate the presence of Ti—N (396.4 eV) and N—Ti—O (397.1 eV) in TiN_xO_{1-x}, while the peaks at 398.4, 399.8, and 400.7 eV are associated with pyridinic-N, pyrrolic-N, and graphitic-N in the NG [45,46], respectively. The change of the Ti—O, Ti—N, and N—Ti—O ratios as well as N/O ratios with nitriding time is presented in Fig. 2e and Table S3. The content of Ti—O decreases sharply, while that of Ti—N increases with nitriding time. However, the N—Ti—O content increases initially from 14.6 % of N-TiO_2/NG to 38.3 % of TiN_xO_{1-x}/NG-5 and then decreases to 23.1 % for TiN_xO_{1-x}/NG-7. TiN_xO_{1-x}/NG-5 has the highest N—Ti—O concentration although TiN_xO_{1-x}/NG-7 shows the largest N/O ratio. These results reveal that TiN_xO_{1-x} solid can be produced from TiO_2 or titania hydrate by thermal nitriding, and the contents of Ti—N, N—Ti—O, and Ti—O species in the TiN_xO_{1-x}/NG can be precisely modulated by varying the nitriding time.

X-ray absorption near-edge spectroscopy (XANES) is carried out to analyze the coordination environment of Ti atoms in TiN_xO_{1-x}/NG-5. For comparison, TiO_2/NG is prepared by annealing of HNTOH/DOE nanosheets under Ar, followed by acid etching of Ni nanoparticles. Fig. 2f displays the Ti K-edge XANES curves of the Ti foil, TiO_2/NG, and TiN_xO_{1-x}/NG-5. The near-edge absorption in TiN_xO_{1-x}/NG-5 shows that the valence of Ti in TiN_xO_{1-x}/NG-5 is less than +4 due to the substitution of O by N. The Fourier transform extended X-ray absorption fine structure (FT-EXAFS) plot (Fig. 2g) reveals that the bond length of Ti—O in the TiN_xO_{1-x}/NG becomes shorter, while the Ti—Ti bond length increases compared to the TiO_2/NG, resulting from the substitution of O by N [47]. In the wavelet transform (WT) image (Fig. 2h), the center of Ti—O in TiN_xO_{1-x}/NG-5 shifts to 4.21 $Å^{-1}$ from 4.69 $Å^{-1}$ (TiO_2/NG), the Ti—Ti coordination is shortened from 5.24 $Å^{-1}$ (TiO_2/NG) to 5.02 $Å^{-1}$, further indicating the formation of N—Ti—O species in TiN_xO_{1-x}/NG-5 [48].

Fig. 3a shows the SEM image of accordion-like TiN_xO_{1-x}/NG-5. The multilayered TiN_xO_{1-x}/NG-5 nanosheets have thicknesses of 6 μm. The energy dispersive X-ray spectroscopy (EDS) elemental maps of TiN_xO_{1-x}/NG-5 show uniform distributions of Ti, O, N, and C (Fig. 3b). The high-resolution transmission electron microscopy (HR-TEM) image of TiN_xO_{1-x}/NG-5 (Fig. 3c) indicates that the amorphous NG monolayer is tightly bonded to the TiN_xO_{1-x} forming layer-by-layer structure. The interplanar lattice distance of 0.21 nm corresponds to the (200) facets of cubic TiN_xO_{1-x} (Fig. 3d) [49]. The layer-by-layer architecture is further confirmed by cross-sectional STEM-EDS line scanning, revealing pronounced periodic oscillations in Ti intensity profiles (Fig. S7). To confirm the presence of sandwiched NG layer within TiN_xO_{1-x}/NG, the TiN_xO_{1-x}/NG-5 is placed in HF solution to remove TiN_xO_{1-x}. The as-produced NG nanosheets resemble the shape of TiN_xO_{1-x}/NG and EDS analysis results display that the presence of C, N and O elements and the Ti element could not be identified, further revealing the NG nanosheets are sandwiched between the TiN_xO_{1-x} layers to form a 2D face-to-face heterostructure (Fig. 3e, f). The thickness of a single TiN_xO_{1-x} and NG nanosheet is measured to be 1.4 and 1.1 nm, respectively (Figs. S8 and S9). Thermogravimetry (TG) analysis of TiN_xO_{1-x}/NG-5 reveals that the NG content is approximately 11.6 wt% (Fig. S10). TEM and AFM images (Figs. S7 and S8b) reveal that voids are observed on the TiN_xO_{1-x} nanosheets after acid etching embedded Ni clusters. The porous TiN_xO_{1-x}

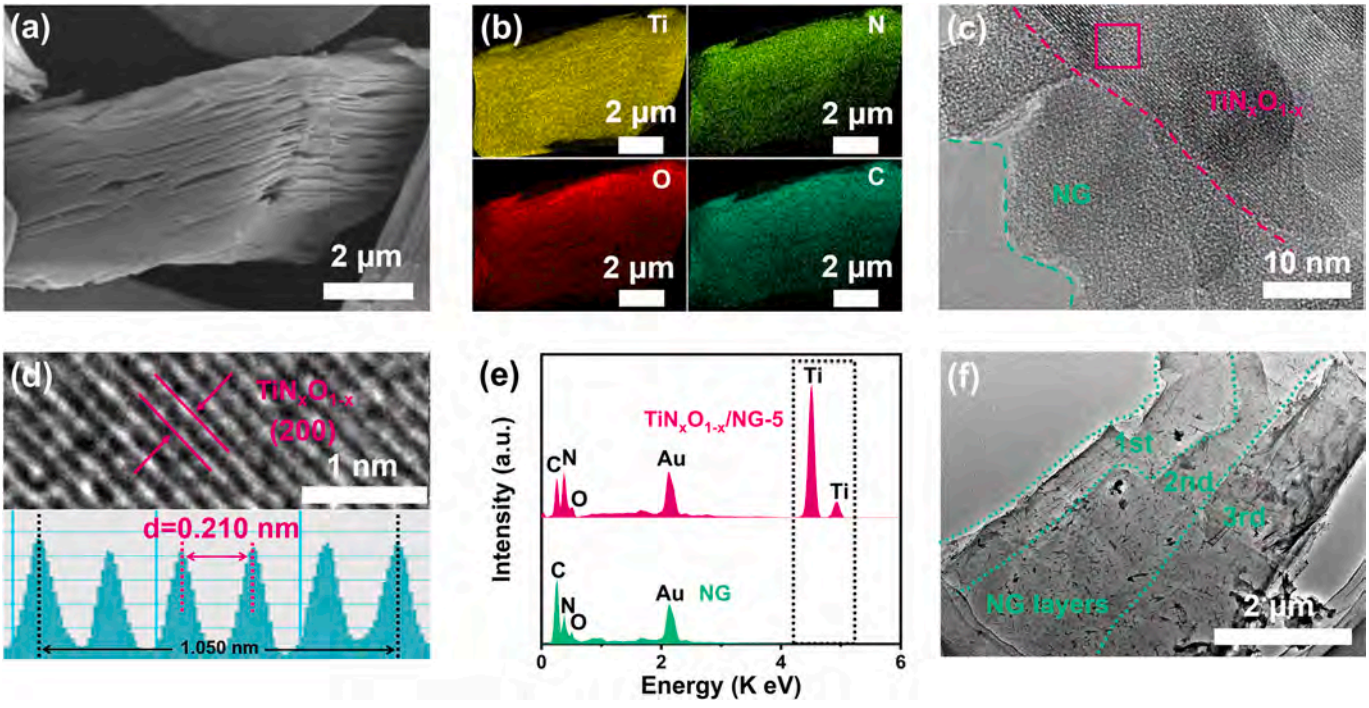

Fig. 3. Morphology, microstructure and chemical compositions of TiN_xO_{1-x}/NG-5 and NG. (a) SEM image, (b) EDS elemental maps, (c) TEM and (d) interplanar spacing and profile of TiN_xO_{1-x}/NG-5; (e) EDS spectra of TiN_xO_{1-x}/NG-5 and NG after etching TiN_xO_{1-x}; (f) TEM image of NG.

$_x$ nanosheets result in large surface area and enriched electrochemical active sites, thus enabling enhanced capacitive storage. For comparison, TiN_xO_{1-x}-5 is prepared by thermal nitriding pure HNTOH nanosheets under 750 °C for 5 h without intercalation of NG. Different from the smooth and multilayered structure of TiN_xO_{1-x}/NG-5, the as-synthesized TiN_xO_{1-x}-5 nanosheets are not complete and show fragments on the surface (Fig. S11), implying that the intercalation of the NG layer effectively prevents the sintering and keeps the structural integrity of TiN_xO_{1-x} during thermal nitridation due to spatial confinement effect. The nitrogen adsorption-desorption curves of TiN_xO_{1-x}/NG-5, TiN_xO_{1-x}-5 and NG are depicted in Fig. S12 and the specific surface areas of TiN_xO_{1-x}/NG-5, TiN_xO_{1-x}-5 and NG are measured to be 123.4, 40.6 and 192.7 $m^2 g^{-1}$, respectively. The pore size distributions show the present of mesopore within TiN_xO_{1-x}/NG-5, TiN_xO_{1-x}-5, NG and the pore volumes are calculated to be 0.31, 0.22 and 0.12 $cm^3 g^{-1}$, respectively. The electrical conductivity of TiN_xO_{1-x}/NG-5 and TiN_xO_{1-x}-5 are measured *via* a power resistivity and compaction density measurement system (Fig. S13), the TiN_xO_{1-x}/NG-5 exhibit a higher conductivity compared to TiN_xO_{1-x}-5 due to the NG intercalation. The alternately stacked TiN_xO_{1-x}/NG-5 heterostructure facilitates fast ion/electron transport during charging/discharging, thereby enabling large pseudocapacitance and high-rate capability.

The capacitive properties of TiN_xO_{1-x}/NG are determined between 0.0 and 0.8 V (*vs.* Ag/AgCl) in 0.5 M H_2SO_4. The cyclic voltammetry (CV) curves of TiN_xO_{1-x}/NG in Fig. 4a display a near-rectangular shape at 20 mV s^{-1}, suggesting excellent capacitive behavior. The CV areas of TiN_xO_{1-x}/NG increase initially and then decrease with nitriding time, and TiN_xO_{1-x}/NG-5 has the largest CV area due to the highest N—Ti—O content. The capacitive and diffusion-controlled contributions were quantified using the Dunn method [50,51] and the results (Fig. S14) show that the charge storage in TiN_xO_{1-x}/NG mainly originates from the surface capacitive behavior. To distinguish the independent contributions of pseudocapacitance and double-layer capacitance, the specific capacitance of TiN_xO_{1-x}/NG-5 is measured by the ion substitution method using several electrolytes with the similar ion concentration such as 1.0 M $[(C_2H_5)_4N]BF_4$, 0.5 M $[(C_2H_5)_4N]_2SO_4$, 0.5 M H_2SO_4, and 1.0 M HBF_4. The $(C_2H_5)_4N^+$ and BF_4^- ions are employed as counter ions

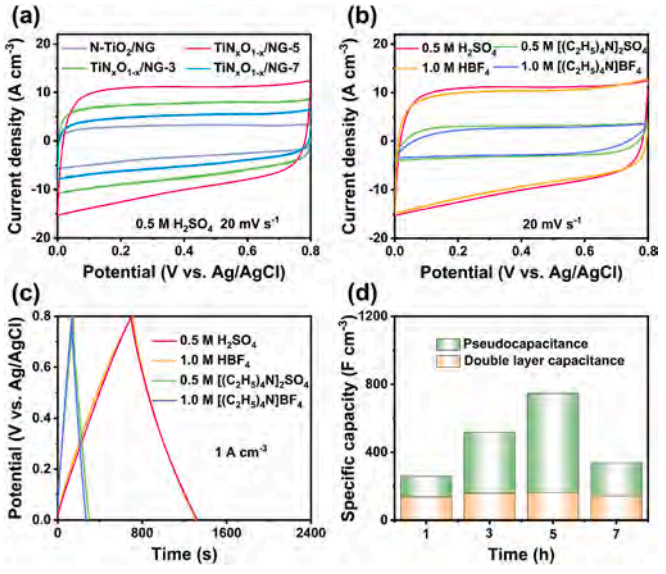

Fig. 4. Capacitive performances of the as-synthesized TiN_xO_{1-x}/NG. (a) CV curves of N-TiO_2/NG, TiN_xO_{1-x}/NG-3, TiN_xO_{1-x}/NG-5, and TiN_xO_{1-x}/NG-7 at 20 mV s^{-1} in 0.5 M H_2SO_4; (b) CV curves and (c) GCD curves of TiN_xO_{1-x}/NG-5 at 20 mV s^{-1} in 0.5 M H_2SO_4, 0.5 M $[(C_2H_5)_4N]_2SO_4$, 1.0 M HBF_4, and 1.0 M $[(C_2H_5)_4N]BF_4$ electrolytes; (d) Contribution of double layer capacitance and pseudocapacitance of N-TiO_2/NG, TiN_xO_{1-x}/NG-3, TiN_xO_{1-x}/NG-5, and TiN_xO_{1-x}/NG-7 at 1 A cm^{-3} in 0.5 M H_2SO_4.

because these ions are known to be redox inert for nitrides or oxynitrides [52,53], therefore, the capacitance in the 1.0 M $[(C_2H_5)_4N]BF_4$ electrolyte is recognized as the double-layer capacitance originating from the electrostatic adsorption and desorption of $(C_2H_5)_4N^+$ and BF_4^- ions. As illustrated in Fig. 4b, the CV plots of TiN_xO_{1-x}/NG-5 in 1.0 M $[(C_2H_5)_4N]BF_4$ and 0.5 M $[(C_2H_5)_4N]_2SO_4$ electrolytes show similar areas, but the CV areas in 0.5 M H_2SO_4 and 1.0 M HBF_4 are much larger, suggesting TiN_xO_{1-x}/NG-5 has a large pseudocapacitance in the acidic electrolytes. The galvanostatic charging/discharging (GCD) curves of TiN_xO_{1-x}/NG-5 in 0.5 M $[(C_2H_5)_4N]_2SO_4$, 1.0 M $[(C_2H_5)_4N]BF_4$, 0.5 M H_2SO_4, and 1.0 M HBF_4 are displayed in Fig. 4c, further revealing that TiN_xO_{1-x}/NG-5 exhibits larger specific capacitance in the acidic electrolyte. The pseudocapacitance originating from the faradaic redox reaction between H^+ and TiN_xO_{1-x} could be obtained by subtracting the double-layer capacitance from the overall capacitance. Fig. 4d and Fig. S15 depict the double layer capacitances and pseudocapacitances of TiN_xO_{1-x}/NG with nitridation time. All the TiN_xO_{1-x}/NG samples have similar double-layer capacitances, whereas the pseudocapacitances increase first and then decrease with nitridation time. Combined with XPS analysis results shown in Fig. 2e, it is reasonable to conclude that the pseudocapacitance of TiN_xO_{1-x}/NG coincides with the variation in N—Ti—O content instead of N/O ratio. Therefore, it is crucial to optimize the content of N—Ti—O instead of N/O ratio to enhance the pseudocapacitive energy storage of metal oxynitrides or nitrides. TiN_xO_{1-x}/NG-5 electrodes with areal mass loading of 1.7, 3.9, 7.6, and 12.3 mg cm^{-2} exhibit large volumetric capacitances of 739.2, 481.5, 371.4, and 329.2 F cm^{-3} at 1 A cm^{-3}, respectively (Fig. S16). When the current density increases from 1 to 20 A cm^{-3}, the TiN_xO_{1-x}/NG-5 electrode with 12.3 mg cm^{-2} mass loading still shows high rate-capability and excellent cycle stability with 94.6 % capacitance retention after 10,000 cycles (Fig. S17).

To investigate the influence of intercalated NG on the capacitive properties of TiN_xO_{1-x}/NG-5, the capacitive characteristics of TiN_xO_{1-x}/NG-5 and TiN_xO_{1-x}-5 are determined in the 0.5 M H_2SO_4 electrolyte. Fig. S18a shows the CV curves of TiN_xO_{1-x}/NG-5 and TiN_xO_{1-x}-5 electrode materials. TiN_xO_{1-x}/NG-5 exhibits a larger CV area than TiN_xO_{1-x}-5, suggesting enhanced capacity due to NG intercalation. Fig. 5a depicts the volumetric specific capacitances with different current densities of TiN_xO_{1-x}/NG-5 and TiN_xO_{1-x}-5 based on the GCD plots in Fig. S18b, c. The volumetric specific capacitances of TiN_xO_{1-x}/NG-5 are measured to be 739.2, 682.6, 619.6, 553.2, and 513.6 F cm^{-3} (gravimetric capacitances of 616.0, 568.8, 516.3, 461.0, and 428.1 F g^{-1}) at 1, 2, 5, 10, and 20 A cm^{-3}, respectively, which are better than those of TiN_xO_{1-x}-5 without NG intercalation (volumetric capacitances of 346.8, 300.1, 241.8, 171.2, and 111.6 F cm^{-3}, gravimetric capacitances of 289.2, 250.1, 201.5, 142.7, and 93.0 F g^{-1}). Moreover, TiN_xO_{1-x}/NG-5 has higher double-layer capacitance (153.9 F cm^{-3}) and pseudocapacitance (585.3 F cm^{-3}) compared with TiN_xO_{1-x}-5 (87.4 F cm^{-3}, 259.4 F cm^{-3}) due to the larger surface area and enriched active sites of TiN_xO_{1-x}/NG-5 (Figs. S18d and S12). Compared to TiN_xO_{1-x}-5, TiN_xO_{1-x}/NG-5 has a larger content of N—Ti—O (Fig. S19 and Table S4) due to carbothermic reduction-assisted thermal nitriding, thereby resulting in higher pseudocapacitance of TiN_xO_{1-x}/NG-5. Moreover, the Nyquist plot of TiN_xO_{1-x}/NG-5 (Fig. S20a) reveals the lower resistance (R_s) of 0.45 Ω and charge transfer resistance (R_{ct}) of 0.67 Ω compared with TiN_xO_{1-x}-5 (R_s = 0.71 Ω, R_{ct} = 1.31 Ω). The EIS Warburg slopes (Fig. S20b) are employed to evaluate H^+ diffusion coefficient (D_{H^+}), which is inversely proportional to the Warburg factor (σ) [54,55]. The TiN_xO_{1-x}/NG-5 electrode (σ = 2.00) demonstrates a significantly lower σ value than TiN_xO_{1-x}-5 electrode (σ = 7.46), suggesting faster ion transport kinetics within the layer-by-layer TiN_xO_{1-x}/NG-5. Fig. 5b and Fig. S21 show that TiN_xO_{1-x}/NG-5 has outstanding long-term stability with capacitance retention of 98.5 % after 10,000 cycles at 1 A cm^{-3} in 0.5 M H_2SO_4, while TiN_xO_{1-x}-5 shows only 13.5 % capacitance retention after 10,000 cycles, suggesting that NG intercalation enhances the cycling stability of TiN_xO_{1-x}. SEM images (Fig. S22a, b) show that the morphology of TiN_xO_{1-x}/NG-5 is

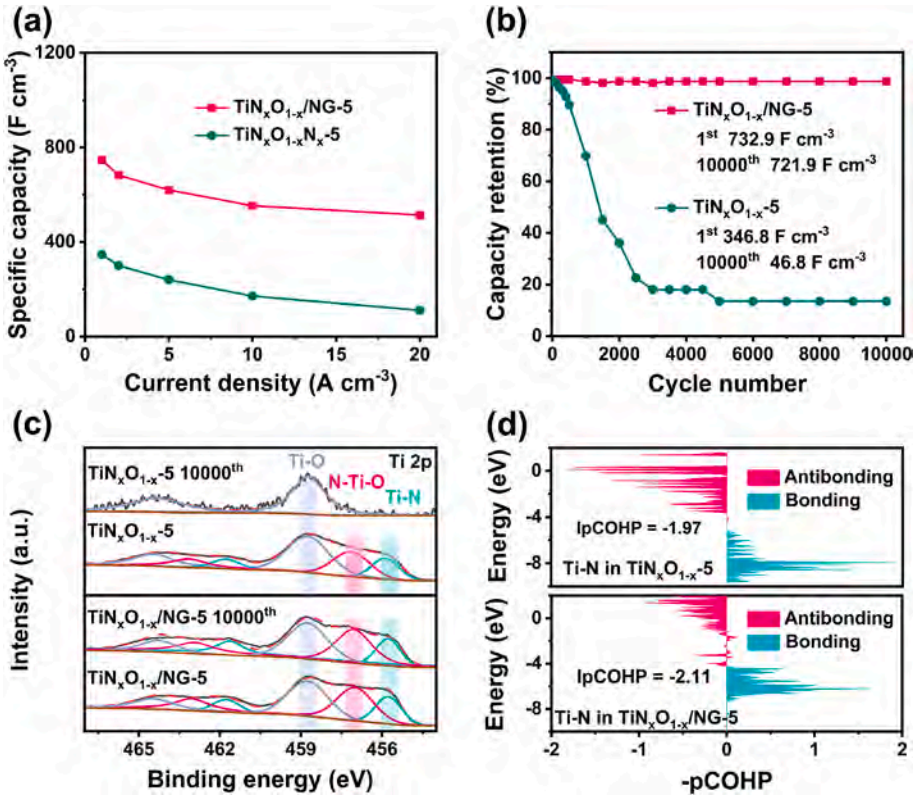

Fig. 5. Rate capability, cycle stability and composition evolutions of TiN_xO_{1-x}/NG-5 and TiN_xO_{1-x}-5. (a) The volumetric capacitances at different current densities, (b) cycling stability at a current density of 1 A cm^{-3}, (c) XPS Ti 2*p* spectra before and after 10,000 cycles and (d) pCOHP and IpCOHP analysis of the TiN_xO_{1-x}/NG-5 and TiN_xO_{1-x}-5.

retained, while the structure of TiN_xO_{1-x}-5 is damaged after 10,000 cycles. The XPS results of TiN_xO_{1-x}/NG-5 and TiN_xO_{1-x}-5 before and after 10,000 cycling are depicted in Fig. 5c and Fig. S22c. Only the Ti—O peak from the cycled TiN_xO_{1-x}-5 electrode is observed and the signals of N—Ti—O and Ti—N disappear, while the Ti 2*p* and N 1*s* spectra of TiN_xO_{1-x}/NG-5 are almost unchanged, further revealing the intercalated NG layers inhibit the electrochemical oxidation of N—Ti—O species. The negative projected crystal orbital Hamiltonian population (pCOHP) is calculated to analyze the Ti—N interaction in TiN_xO_{1-x} with and without NG intercalation (Fig. 5d). Compared to TiN_xO_{1-x}-5, the occupation of anti-bonding states below the Fermi level (E_F) of TiN_xO_{1-x}/NG-5 decreases, suggesting the strong interfacial electron interactions between NG and TiN_xO_{1-x} [56]. The calculated integrated pCOHP value of Ti—N in TiN_xO_{1-x}/NG-5 is −2.11 eV, which is smaller than that in TiN_xO_{1-x}-5 (−1.97 eV), indicating a more stable Ti—N bond in TiN_xO_{1-x}/NG-5. These results indicate that the intercalated NG layers effectively prevent electrochemical oxidation of TiN_xO_{1-x} thereby enabling long-term electrochemical stability of TiN_xO_{1-x}/NG in acidic electrolytes.

To elucidate the pseudocapacitive energy storage mechanism, an *in situ* EQCM (Fig. S23) is utilized to track the dynamic mass changes of the electrode during charging and discharging. Fig. 6a shows the mass change of the TiN_xO_{1-x}/NG-5-coated EQCM electrode during CV at 10 mV s^{-1} in the 0.0 –0.8 V potential based on Sauerbrey's equation [57]. During cathodic scanning (discharging), the mass of TiN_xO_{1-x}/NG-5 increases monotonically due to the insertion of H^+. In contrast, the mass decreases nearly to the initial value during anodic scanning (charging) due to the desertion of H^+. *In situ* Raman scattering and *in situ* ATR-FTIR measurements (Fig. S24) are performed to monitor the evolution of the electrodes during the cathodic/anodic scanning process. Fig. 6b shows the *in situ* Raman spectroscopic evolution at different potentials during cycling. The band at 405 cm^{-1} stemming from the B_{1g} mode of the N—Ti—O bond gradually shifts to larger wavenumbers with increasing potential (charging) and shifts back to approximately the initial value with decreasing potential (discharging), while the E_g mode of the Ti—O bond remains unchanged. Meanwhile, Fig. S25 shows that the N—Ti—O intensity in the Raman spectroscopy exhibits periodic variations, suggesting reversible changes in N—Ti—O bond length due to H^+ desertion/insertion during charging/discharging. Fig. 6c displays the *in situ* FTIR spectra of TiN_xO_{1-x}/NG-5 during charging/discharging. The peaks at 1050 and 1185 cm^{-1} correspond to the stretching vibration modes of the Ti—N and N—Ti—O bonds, respectively [58]. Notably, the bond length of N—Ti—O gradually shortens during the anodic scanning and reversibly increases during the cathodic scanning processes. These results confirm that pseudocapacitive charge storage of TiN_xO_{1-x}/NG-5 arises from H^+ desertion/insertion on TiN_xO_{1-x}/NG-5 by the N—Ti—O species active center. *Ex situ* XPS is carried out to evaluate the evolution of the surface chemical species during charging and discharging. As shown in C 1*s* and N 1*s* spectra at different charge/discharge states (Fig. S26), the C—N bonding peak from NG in C 1*s* and the pyridinic-N, pyrrolic-N, and graphitic-N peaks from NG in N 1*s* have no obvious shift during the cathodic/anodic scanning process, indicating that the pseudocapacitive contribution from NG is negligible. By contrast, the Ti 2*p* XPS spectra of the N—Ti—O bond in Fig. 6d exhibits a reversible shift, whereas Ti—N and Ti—O bonds show negligible changes during cycling, in line with *in situ* Raman and FTIR results. Therefore, it is reasonable to conclude that the pseudocapacitive redox activity arises from surface interactions between H^+ ions and N—Ti—O species, accompanied by the reversible change of Ti valence state. The corresponding reversible redox process for TiN_xO_{1-x} charge storage in an acidic electrolyte could be expressed by the following equation:

$$Ti^{\delta}N_xO_{1-x} + H^+ + e^- \leftrightarrow Ti^{\delta-1}N_xO_{1-x}(H)$$

In order to gain a deeper understanding of the active sites on TiN_xO_{1-x}/NG-5, SCN^- recognized as a metal-centered active site inhibitor is

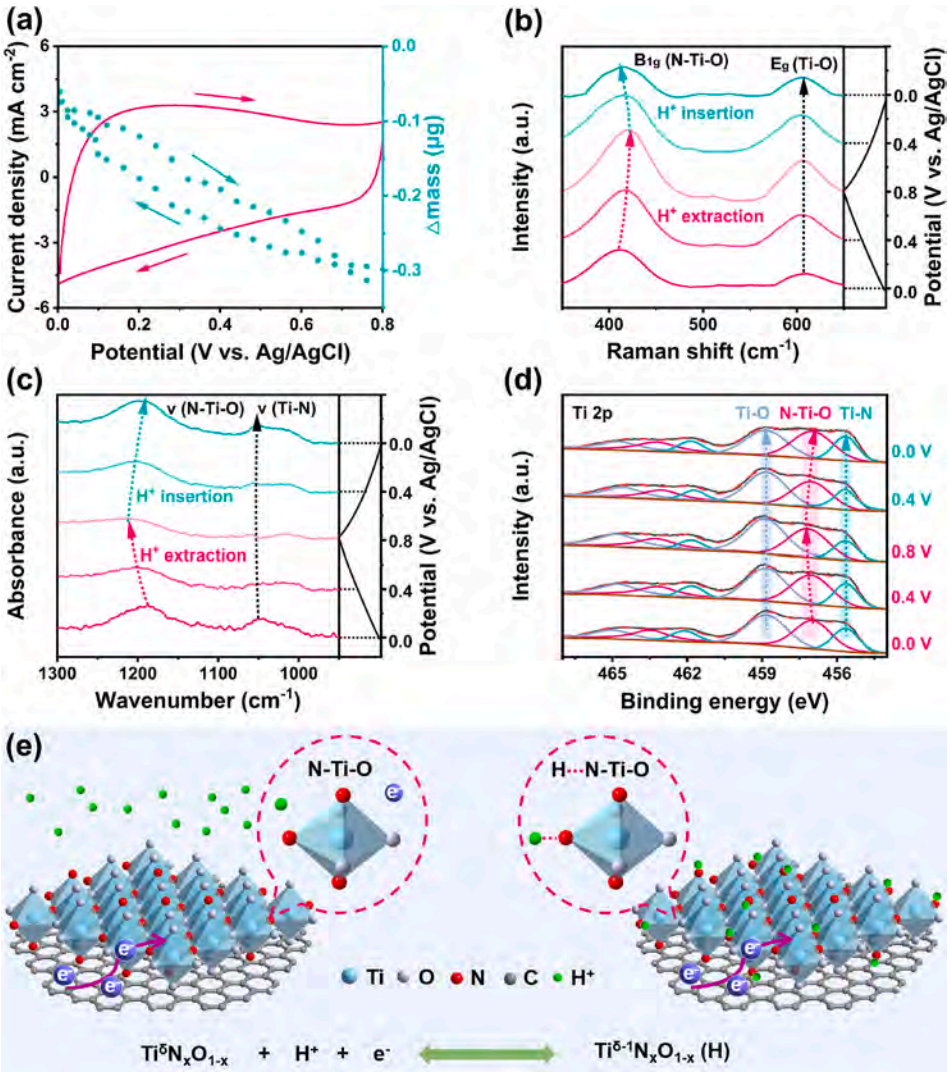

Fig. 6. *In-situ* EQCM, Raman, FT-IR, XPS spectra and schematic illustration pseudocapacitive energy storage mechanism of TiN_xO_{1-x}/NG-5 during charging/discharging. (a) Plots of CV and mass change (Δm, μg) *versus* potential of the TiN_xO_{1-x}/NG-5 electrode on quartz acquired from the EQCM frequency response at 10 mV s^{-1}; (b) *In situ* Raman scattering spectra, (c) *in situ* FTIR spectra, and (d) *ex situ* XPS spectra of TiN_xO_{1-x}/NG-5 at different potentials during CV measurement at 1 mV s^{-1}; (e) Schematic illustration of H^+ storage in the TiN_xO_{1-x}/NG during charging/discharging.

introduced into the 0.5 M H_2SO_4 electrolyte [59]. As shown in Fig. S27, the redox peaks of TiN_xO_{1-x}/NG-5 at around 0.6 V remain unchanged in the CV curves at a scanning rate of 1 mV s^{-1} after the addition of SCN^- ions, suggesting that the Ti of N—Ti—O species is not the active center in pseudocapacitive charge storage. Density functional theory (DFT) calculations are carried out to further identify the active sites for pseudocapacitive charge storage in TiN_xO_{1-x}/NG. The heterointerface model with single-layer TiN_xO_{1-x} and NG is constructed (Fig. S28). The N site has a higher H^+ adsorption energy (E_{H+}) compared with O site in N—Ti—O, suggesting the N sites in N—Ti—O species are the active sites for pseudocapacitive charge storage originating from H^+ desertion/insertion reactions during cycling. The N sites in the TiN_xO_{1-x}/NG have a higher E_{H+} of −3.72 eV than the N sites in TiN_xO_{1-x} (−2.16 eV), indicating stronger H^+ adsorption at the TiN_xO_{1-x}/NG heterointerface. Compared to TiN_xO_{1-x}, the electron transfer from the NG layer to the TiN_xO_{1-x} layer further enhance the interactions between H^+ and N—Ti—O species in TiN_xO_{1-x}/NG (Fig. 6e), thus enabling much improved pseudocapacitance and rate capability.

The all-solid-state symmetrical devices comprising the TiN_xO_{1-x}/NG-5 electrodes and H_2SO_4/PVA gel electrolyte are assembled to assess the application potential (Fig. S29a). The CV plots at scanning rates from 5 to 100 mV s^{-1} show a similar shape without obvious distortion, corroborating the excellent capacitive behavior (Fig. S29b). The device has a high discharge capacitance of 342.6 F cm^{-3} (285.5 F g^{-1}) at a current density of 1 A cm^{-3} and shows a high energy density of 47.6 mWh cm^{-3} (39.8 Wh kg^{-1}) and power density of 500.0 W cm^{-3} (416.7 W kg^{-1}) (Fig. S29c), which outperform previously reported metal nitride or oxynitride supercapacitors (Fig. S29d, Table S1) [17,20,60–66]. The device also shows excellent cycling stability with 91.3 % capacity retention after 10,000 cycles (Fig. S29e, f). The CV curves of single and two cells in series acquired at 20 mV s^{-1} are shown in Fig. S29g, the whole potential of the two cells in series is 2.0 V, which is twice that of single device. Two SCs connected in series can illuminate a commercial red light-emitting-diode (LED) with a voltage of 2.0 V (Fig. S29h), and it can continue to light for 12 min after charging (Fig. S29i), demonstrating the promising practical aspect of TiN_xO_{1-x}/NG in electrochemical energy storage.

3. Conclusions

2D TiN_xO_{1-x} nanosheets intercalated with nitrogen-doped graphene (TiN_xO_{1-x}/NG) are controllably fabricated by thermal nitriding of 1,8-diaminooctane intercalated $H_{0.8}Ni_{0.4}Ti_{1.6}O_4{\cdot}H_2O$ nanosheets under ammonia at 750 °C. The $H_{0.8}Ni_{0.4}Ti_{1.6}O_4{\cdot}H_2O$ layers are transformed

into TiN_xO_{1-x} nanosheets after Ni etching, and the sandwiched 1,8-diaminooctane is carbonized into NG by confined thermal nitriding, resulting in the formation of layer-by-layer TiN_xO_{1-x}/NG nanosheets. *In situ* EQCM, Raman scattering, FTIR, and *ex situ* XPS combined with DFT calculations reveal that the pseudocapacitance originates from the Faradic reaction between H^+ and N active sites of N—Ti—O within TiN_xO_{1-x}/NG, accompanied by the Ti valence state change. The pseudocapacitance of TiN_xO_{1-x}/NG in H_2SO_4 depends on the N—Ti—O content instead of the N/O ratio reported in the literature. The intercalated NG not only serves as the conductive layer and electron donor to enhance electron transport and H^+ adsorption at the N sites of N—Ti—O, but also inhibits the electrochemical oxidation of TiN_xO_{1-x}, thereby giving rise to superior pseudocapacitive capacity and excellent cycling stability. The TiN_xO_{1-x}/NG electrode shows a remarkable volumetric capacitance of 739.2 F cm^{-3} (616.0 F g^{-1}) at 1 A cm^{-3}, rate capability of 513.6 F cm^{-3} (428.1 F g^{-1}) at 20 A cm^{-3}, and excellent cycling stability with 98.5 % capacitance retention after 10,000 cycles, which are better than those of previously reported metal oxynitrides. The symmetrical all-solid-state flexible SC consisting of the TiN_xO_{1-x}/NG-5 electrodes and gel polymer H_2SO_4/PVA electrolyte has a high energy density of 47.6 mWh cm^{-3} (39.8 Wh kg^{-1}) at a power density of 500.0 mW cm^{-3} (416.7 W kg^{-1}). This work clarifies the pseudocapacitive storage mechanism of TiN_xO_{1-x} and offers insights into the development of nonlayered metal oxynitrides for supercapacitors.

CRediT authorship contribution statement

Xiuli Li: Writing – original draft, Methodology, Investigation, Formal analysis, Data curation. **Rui Huo:** Methodology, Investigation, Formal analysis, Data curation. **Zihuan Tang:** Investigation, Formal analysis, Data curation. **Yulei Ren:** Investigation, Formal analysis, Data curation. **Hao Song:** Writing – review & editing, Methodology, Formal analysis, Data curation. **Paul K. Chu:** Writing – review & editing. **Kaifu Huo:** Writing – review & editing, Supervision, Methodology, Funding acquisition, Conceptualization.

Declaration of competing interest

The authors declare that they have no known competing financial interests or personal relationships that could have appeared to influence the work reported in this paper.

Acknowledgments

This work was financially supported by the National Natural Science Foundation of China (U2004210), City University of Hong Kong Donation Research Grants (DON-RMG 9229021). The authors are grateful for the facility support provided by the Analytical and Testing Center of WUST and Jianping Li of the Institute of Advanced Materials and Nanotechnology in WUST for the Raman scattering analysis.

Appendix A. Supplementary data

Supplementary data to this article can be found online at https://doi.org/10.1016/j.cej.2025.164579.

Data availability

Data will be made available on request.

References

[1] J. Huang, Y.P. Xie, Y. You, J.L. Yuan, Q.Q. Xu, H.B. Xie, Y.W. Chen, Rational design of electrode materials for advanced supercapacitors: from lab research to commercialization, Adv. Funct. Mater. 33 (2023) 2213095, https://doi.org/10.1002/adfm.202213095.

[2] B.G. Zhao, G.Q. Suo, R.R. Mu, C.J. Lin, J.R. Li, X.J. Hou, X.H. Ye, Y.L. Yang, L. Zhang, Confining WS_2 hierarchical structures into carbon core-shells for enhanced sodium storage, J. Colloid Interface Sci. 677 (2025) 637–646, https://doi.org/10.1016/j.jcis.2024.08.115.

[3] R.R. Mu, G.Q. Suo, C.J. Lin, J.R. Li, S. Javed, X.J. Hou, X.H. Ye, Y.L. Yang, L. Zhang, Cobalt-doped copper sulfide nanocomposite integrated with graphene oxide as a high-performance conversion anode for aqueous zinc-ion batteries, Chem. Eng. J. 498 (2024) 155816, https://doi.org/10.1016/j.cej.2024.155816.

[4] G.Q. Suo, B.G. Zhao, R.R. Mu, C.J. Lin, S. Javed, X.J. Hou, X.H. Ye, Y.L. Yang, L. Zhang, Dual carbon confined MoS_2 hierarchical microspheres as high-performance anode for sodium-ion batteries with superior cycling stability, J. Energy Storage 77 (2024) 109801, https://doi.org/10.1016/j.est.2023.109801.

[5] S. Chakraborty, K.E. Battioui, T. Beke-Somfai, Peptide-based assemblies for supercapacitor applications, Small Sci. 4 (2024) 2300217, https://doi.org/10.1002/smsc.202300217.

[6] K.A. Sammed, A. Kumar, A. Farid, W.B. Zhang, A.R. Akbar, M. Ali, S. Ajmal, G. Yasin, N. Ullah, L.J. Pan, W. Zhao, Exploration of the role of oxygen-deficiencies coupled with Ni-doped V_2O_5 nanosheets anchored on carbon nanocoils for high-performance supercapacitor device, Chem. Eng. J. 486 (2024) 150388, https://doi.org/10.1016/j.cej.2024.150388.

[7] Z.Z. Zhai, B. Ren, Y.L. Xu, Nitrogen self-doped carbon aerogels from chitin for supercapacitors, J. Power Sources 481 (2021) 228976, https://doi.org/10.1016/j.jpowsour.2020.228976.

[8] L.N. Shi, X.Z. Li, L.T. Cui, P.F. Wang, T.F. Yi, Recent progresses and perspectives of VN-based materials in the application of electrochemical energy storage, J. Ind. Eng. Chem. 114 (2022) 52–76, https://doi.org/10.1016/j.jiec.2022.07.045.

[9] P. Simon, Y. Gogotsi, Materials for electrochemical capacitors, Nat. Mater. 7 (2008) 845–854, https://doi.org/10.1038/nmat2297.

[10] S. Balasubramaniam, A. Mohanty, S.K. Balasingam, S.J. Kim, A. Ramadoss, Comprehensive insight into the mechanism, material selection and performance evaluation of supercapatteries, Nano-Micro Lett. 12 (2020) 1–46, https://doi.org/10.1007/s40820-020-0413-7.

[11] D. Patra, S.K. Pati, S. Muduli, S. Mishra, S. Park, Highly planar pseudocapacitive semiconducting polymer electrodes toward symmetric supercapacitors with a wide range of operating potentials, Chem. Eng. J. 482 (2024) 149162, https://doi.org/10.1016/j.cej.2024.149162.

[12] H. Wang, J.M. Li, K. Li, Y.P. Lin, J.M. Chen, L.J. Gao, V. Nicolosi, X. Xiao, J.M. Lee, Transition metal nitrides for electrochemical energy applications, Chem. Soc. Rev. 50 (2021) 1354–1390, https://doi.org/10.1039/D0CS00415D.

[13] Q. Luo, C. Lu, L. Liu, M. Zhu, A review on the synthesis of transition metal nitride nanostructures and their energy related applications, Green Energy Environ. 8 (2023) 406–437, https://doi.org/10.1016/j.gee.2022.07.002.

[14] A. Joseph, T. Thomas, Recent advances and prospects of metal oxynitrides for supercapacitor, Prog. Solid State Chem. 68 (2022) 100381, https://doi.org/10.1016/j.progsolidstchem.2022.100381.

[15] J.L. Zhang, Y. Li, Y. Zhang, X.Y. Qian, R.C. Niu, R.D Hu, X.F. Zhu, X. Wang, J. W. Zhu, The enhanced adhesion between overlong TiN_xO_y/MnO_2 nanoarrays and Ti substrate: Towards flexible supercapacitors with high energy density and long service life, Nano Energy 43 (2018) 91–102, https://doi.org/10.1016/j.nanoen.2017.11.013.

[16] X.N. Pan, B.J. Xi, H.B. Lu, Z.C.Y. Zhang, X.G. An, J. Liu, J.K. Feng, S.L. Xiong, Molybdenum oxynitride atomic nanoclusters bonded in nanosheets of N-doped carbon hierarchical microspheres for efficient sodium storage, Nano-Micro Lett. 14 (2022) 163, https://doi.org/10.1007/s40820-022-00893-7.

[17] X.Q. Cheng, Z.H. Pan, J. Yang, Y.T. Zhang, X.S. Wang, C.C. Ye, J.C. Zhuang, Q. M. Huang, Y.C. Qiu, W.S. Li, Tungsten oxynitride nanowires as negative electrode for fiber-shaped supercapacitor, J. Power Sources 427 (2019) 243–249, https://doi.org/10.1016/j.jpowsour.2019.04.097.

[18] T.Z. Xiong, J.T. Li, J.C. Roy, M. Koroma, Z.X. Zhu, H. Yan, L. Zhang, T. Ouyang, M. S. Balogun, M. Al-Mamun, Hetero-interfacial nickel nitride/vanadium oxynitride porous nanosheets as trifunctional electrodes for HER, OER and sodium ion batteries, J. Energy Chem. 81 (2023) 71–81, https://doi.org/10.1016/j.jechem.2023.01.064.

[19] F.Z. Ye, W. Yang, X.B. Liao, C.H. Dong, L. Xu, L.Q. Mai, A micro battery supercapacitor hybrid device with ultrahigh cycle lifespan and power density enabled by bi-functional coating design, Adv. Funct. Mater. 35 (2025) 2413379, https://doi.org/10.1002/adfm.202413379.

[20] N.N. Sun, J. Xu, Y.P. Su, P. Jiang, Y.Z. Zou, W.W. Liu, M.X. Wang, D.Y. Zhou, Energy storage performance of in-situ grown titanium nitride current collector/titanium oxynitride laminated thin film electrodes, Chem. Eng. J. 474 (2023) 145603, https://doi.org/10.1016/j.cej.2023.145603.

[21] H. Tan, Z. Liu, D. Chao, P. Hao, D. Jia, Y. Sang, H. Liu, H.J. Fan, Partial nitridation-induced electrochemistry enhancement of ternary oxide nanosheets for fiber energy storage device, Adv. Energy Mater. 8 (2018) 1800685, https://doi.org/10.1002/aenm.201800685.

[22] J. Yu, Y. Wang, L. Mou, D. Fang, S. Chen, S. Zhang, Nature-inspired 2D-mosaic 3D-gradient mesoporous framework: bimetal oxide dual-composite strategy toward ultrastable and high-capacity lithium storage, ACS Nano 12 (2018) 2035–2047, https://doi.org/10.1021/acsnano.8b00168.

[23] S.Z. Wang, L.L. Li, Y.L. Shao, L. Zhang, Y.L. Li, Y.Z. Wu, X.P. Hao, Transition-metal oxynitride: a facile strategy for improving electrochemical capacitor storage, Adv. Mater. 31 (2019) 1806088, https://doi.org/10.1002/adma.201806088.

[24] P. Mouchani, R. Sarraf-Mamoorya, H. Aghajani, Preparation of titanium nitride/oxynitride nanotube array via ammonia-free PECVD method for enhancing supercapacitor performance, J. Alloys Compd. 904 (2022) 163895, https://doi.org/10.1016/j.jallcom.2022.163895.

[25] L.T. Yan, G. Chen, S. Tan, M. Zhou, G.F. Zou, S.G. Deng, S.N. Smirnov, H.M. Luo, Titanium oxynitride nanoparticles anchored on carbon nanotubes as energy storage materials, ACS Appl. Mater. Interfaces 7 (2015) 24212–24217, https://doi.org/10.1021/acsami.5b07630.

[26] M.Y. Ma, H. Zhao, Y. Li, Y.X. Zhang, J.L. Bai, X.M. Mu, J.Y. Zhou, Y.M. He, E. Q. Xie, Synthesis of high-performance TiN based battery-type wire supercapacitors and their energy storage mechanisms, Electrochim. Acta 334 (2020) 135543, https://doi.org/10.1016/j.electacta.2019.135543.

[27] E.J. Lee, L. Lee, M.A. Abbas, J.H. Bang, The influence of surface area, porous structure, and surface state on the supercapacitor performance of titanium oxynitride: implications for a nanostructuring strategy, Phys. Chem. Chem. Phys. 19 (2017) 21140–21151, https://doi.org/10.1039/C7CP03546B.

[28] S. Panda, K. Deshmukh, S.K.K. Pasha, J. Theerthagiri, S. Manickam, M.Y. Choi, MXene based emerging materials for supercapacitor applications: recent advances, challenges, and future perspectives, Coord. Chem. Rev. 462 (2022) 214518, https://doi.org/10.1016/j.ccr.2022.214518.

[29] Q.Z. Zhu, J.P. Li, P. Simon, B. Xu, Two-dimensional MXenes for electrochemical capacitor applications: progress, challenges and perspectives, Energy Storage Mater. 35 (2021) 630–660, https://doi.org/10.1016/j.ensm.2020.11.035.

[30] Y.S. Zhou, W. Guo, T. Li, A review on transition metal nitrides as electrode materials for supercapacitors, Ceram. Int. 45 (2019) 21062–21076, https://doi.org/10.1016/j.ceramint.2019.07.151.

[31] A. Djire, O.T. Ajenifujah, A.E.S. Sleightholme, P. Rasmussen, L.T. Thompson, Effects of surface oxygen on charge storage in high surface area early transition-metal carbides and nitrides, J. Power Sources 275 (2015) 159–166, https://doi.org/10.1016/j.jpowsour.2014.10.161.

[32] D. Groult, C. Mercey, B. Raveau, Nouveaux oxydes à structure en feuillets: les titanates de potassium non-stoechiométriques $K_x(M_yTi_{2-y})O_4$, J. Solid State Chem. 32 (1980) 289–296, https://doi.org/10.1016/S0022-4596(80)80022-3.

[33] D. Yang, Q.U. Hassan, Q.W. Chen, H.D. Yang, M. Bilal, S. Afzal, J.P. Zhou, Development of novel $K_{0.8}Ni_{0.4}Ti_{1.6}O_4$ nano bamboo leaves, microstructural characterization, double absorption, and photocatalytic removal of organic pollutant, Environ. Res. 211 (2022) 113118, https://doi.org/10.1016/j.envres.2022.113118.

[34] T. Sasaki, F. Kooli, M. Iida, Y. Michiue, S. Takenouchi, Y. Yajima, F. Izumi, B. C. Chakoumakos, M. Watanabe, A mixed alkali metal titanate with the lepidocrocite-like layered structure. Preparation, crystal structure, protonic form, and acid-base intercalation properties, Chem. Mater. 10 (1998) 4123–4128, https://doi.org/10.1021/cm980535f.

[35] W.W. Fu, Y.T. Li, M.S. Chen, Y.J. Hu, B.H. Liu, K. Zhang, C.Y. Zhan, M. Zhang, Z. R. Shen, An orderly arrangement of layered carbon Nanosheet/TiO_2 nanosheet stack with superior artificially interfacial lithium pseudocapacity, J. Power Sources 468 (2020) 228363, https://doi.org/10.1016/j.jpowsour.2020.228363.

[36] Q.W. Li, Y. Chen, J.B. Zhang, W.F. Tian, L. Wang, Z.G. Ren, X.C. Ren, X.X. Li, B. Gao, X. Peng, P.K. Chu, K.F. Huo, Spatially confined synthesis of vanadium nitride nanodots intercalated carbon nanosheets with ultrahigh volumetric capacitance and long life for flexible supercapacitors, Nano Energy 51 (2018) 128–136, https://doi.org/10.1016/j.nanoen.2018.06.053.

[37] Y.B. Shan, X.F. Yue, J.J. Chen, J.K. Han, G. Ekoya, L.G. Hu, R. Liu, Z.Z. Qiu, C. X. Cong, Revealing layer-dependent interlayer interactions by doping effect on graphene in WSe_2/N-layer graphene heterostructures using Raman and photoluminescence spectroscopy, Rare Metals 41 (2022) 3646–3653, https://doi.org/10.1007/s12598-022-02053-7.

[38] E.B. Zhang, S.S. Ding, X.P. Li, X.Y. Ma, X.Q. Gao, L. Liu, Y.T. Shen, S.Y. Cheng, W. B. Mi, Y.L. Zhou, G.Y. Feng, Y.R. Song, X.J. Li, Y.J. Xue, K.Y. Xin, X. Zeng, Q. Y. Jiang, R.F. Zhang, X.F. Liu, Z.M. Wei, Q.D. Zeng, B. Wang, Q.F. Li, J. Liu, J. Yan, S.B. Lei, Y.L. Yang, W.P. Hu, Graphene rolls with tunable chirality, Nat. Mater. 24 (2025) 377–383, https://doi.org/10.1038/s41563-025-02127-8.

[39] T.T. Chen, H.P. Liu, Y.J. Wei, I.C. Chang, M.H. Yang, Y.S. Lin, K.L. Chan, H. T. Chiub, C.Y. Lee, Porous titanium oxynitride sheets as electrochemical electrodes for energy storage, Nanoscale 6 (2014) 5106–5109, https://doi.org/10.1039/C4NR00101J.

[40] M. Sluban, P. Umek, Z. Jaglicic, J. Buh, P. Smitek, A. Mrzel, C. Bittencourt, P. Guttmann, M.H. Delville, D. Mihailovic, D. Arcon, Controlling disorder and superconductivity in titanium oxynitride nanoribbons with anion exchange, ACS Nano 9 (2015) 10133–10141, https://doi.org/10.1021/acsnano.5b03742.

[41] J.S. Samdani, T.H. Kang, B.J. Lee, Y.H. Jang, J.S. Yu, S. Shanmugam, Heterostructured titanium oxynitride-manganese cobalt oxide nanorods as high-performance electrode materials for supercapacitor devices, ACS Appl. Mater. Interfaces 12 (2020) 54524–54536, https://doi.org/10.1021/acsami.0c13803.

[42] R. Asahi, T. Morikawa, T. Ohwaki, K. Aoki, Y. Taga, Visible-light photocatalysis in nitrogen-doped titanium oxides, Science 293 (2001) 269–271, https://doi.org/10.1126/science.1061051.

[43] Y. Sun, Y.G. Su, Z.B. Zhao, J.X. Zhao, M.S. Ye, X.R. Wen, Capacitive heavy metal ion removal of 3D self-supported nitrogen-doped carbon-encapsulated titanium nitride nanorods via the synergy of faradic-reaction and electro-adsorption, Chem. Eng. J. 443 (2022) 136542, https://doi.org/10.1016/j.cej.2022.136542.

[44] H. Chen, C.L. Dai, Y.N. Li, R.M. Zhan, M.Q. Wang, B.S. Guo, Y.Q. Zhang, H. Liu, M. W. Xu, S.J. Bao, An excellent full sodium-ion capacitor derived from a single Ti-based metal-organic framework, J. Mater. Chem. A 6 (2018) 24860–24868, https://doi.org/10.1039/C8TA09072F.

[45] G.H. Chen, B. Feng, G.C. Xu, Q.H. Gong, L.J. Yan, C.K. Zhou, J.T. Jiang, L.J. Yang, Q. Wu, X.Z. Wang, Z. Hu, Bismuth confined in thick nitrogen-doped carbon for durable low-temperature potassium-ion batteries, ACS Energy Lett. 10 (2025) 1821–1828, https://doi.org/10.1021/acsenergylett.4c03489.

[46] S.X. Zhai, K. Li, C.C. Li, C. Zhai, Q. Han, Z.Y. Zhang, Y.N. Fu, X.Y. Li, K.L. Jin, Z. S. Cai, Y.P. Zhao, Lignin-derived N, S-codoped hierarchical porous carbons with high mesoporous rate for sustainable supercapacitive energy storage, J. Energy Storage 85 (2024) 111036, https://doi.org/10.1016/j.est.2024.111036.

[47] C.W. Liu, D. Hao, J. Ye, S. Ye, F.L. Zhou, H.B. Xie, G.W. Qin, J.T. Xu, J. Liu, S. Li, C. H. Sun, Knowledge-driven design and lab-based evaluation of B-doped TiO_2 photocatalysts for ammonia synthesis, Adv. Energy Mater. 13 (2023) 2204126, https://doi.org/10.1002/aenm.202204126.

[48] B.X. Ni, G.R. Zhang, H.M. Wang, Y.L. Min, K. Jiang, H.X. Li, Correlating oxidation state and surface ligand motifs with the selectivity of CO_2 photoreduction to C_2 products, Angew. Chem. Int. Ed. 62 (2023) e202215574, https://doi.org/10.1002/ange.202215574.

[49] C.R. Zhu, P.H. Yang, D.L. Chao, X.L. Wang, X. Zhang, S. Chen, B.K. Tay, H. Huang, H. Zhang, W.J. Mai, H.J. Fan, All metal nitrides solid-state asymmetric supercapacitors, Adv. Mater. 27 (2015) 4566–4571, https://doi.org/10.1002/adma.201501838.

[50] J. Wang, J. Polleux, J. Lim, B. Dunn, Pseudocapacitive contributions to electrochemical energy storage in TiO_2 (anatase) nanoparticles, J. Phys. Chem. C 111 (2007) 14925–14931, https://doi.org/10.1021/jp074464w.

[51] D.P. Dubal, S. Abdel-Azeim, N.R. Chodankar, Y.K. Han, Molybdenum nitride nanocrystals anchored on phosphorus-incorporated carbon fabric as a negative electrode for high-performance asymmetric pseudocapacitor, IScience 16 (2019) 50–62, https://doi.org/10.1016/j.isci.2019.05.018.

[52] P. Pandea, P.G. Rasmussena, L.T. Thompson, Charge storage on nanostructured early transition metal nitrides and carbides, J. Power Sources 207 (2012) 212–215, https://doi.org/10.1016/j.jpowsour.2012.01.028.

[53] C. Huang, P. Qin, D. Li, Q.D. Ruan, H. Song, L.L. Liu, Y.Z. Wu, Y.H. Ma, Q.W. Li, K. F. Huo, P.K. Chu, Origin of superior pseudocapacitive mechanism of transition metal nitrides, J. Energy Chem. 69 (2022) 561–568, https://doi.org/10.1016/j.jechem.2022.01.041.

[54] J. Zhou, A.Q. Dong, L. Du, C.C. Yang, L. Ye, X. Wang, L.J. Zhao, Q. Jiang, Mn-doped ZnO microspheres as cathode materials for aqueous zinc ion batteries with ultrastability up to 10000 cycles at a large current density, Chem. Eng. J. 421 (2021) 127770, https://doi.org/10.1016/j.cej.2020.127770.

[55] Z.K. Ma, J.W. Chen, J. Vatamanu, O. Borodin, D. Bedrov, X.G. Zhou, W.G. Zhang, W.S. Li, K. Xu, L.D. Xing, Expanding the low-temperature and high-voltage limits of aqueous lithium-ion battery, Energy Storage Mater. 45 (2022) 903, https://doi.org/10.1016/j.ensm.2021.12.045.

[56] X.K. Huang, H.X. Xu, D. Cao, D.J. Cheng, Interface construction of P-substituted MoS_2 as efficient and robust electrocatalyst for alkaline hydrogen evolution reaction, Nano Energy 78 (2020) 105253, https://doi.org/10.1016/j.nanoen.2020.105253.

[57] J.W. Chen, P.S. Lee, Electrochemical supercapacitors: from mechanism understanding to multifunctional applications, Adv. Energy Mater. 11 (2021) 2003311, https://doi.org/10.1002/aenm.202003311.

[58] G.H. Tian, Y.Y. Chen, K. Pan, D.J. Wang, W. Zhou, Z.Y. Ren, H.G. Fu, Efficient visible light-induced degradation of phenol on N-doped anatase TiO_2 with large surface area and high crystallinity, Appl. Surf. Sci. 256 (2010) 3740–3745, https://doi.org/10.1016/j.apsusc.2010.01.016.

[59] D. Zhao, K.A. Sun, W.C. Cheong, L.R. Zheng, C. Zhang, S.J. Liu, X. Cao, K.L. Wu, Y. Pan, Z.W. Zhuang, B.T. Hu, D.S. Wang, Q. Peng, C. Chen, Y.D. Li, Synergistically interactive pyridinic-N-MoP sites: identified active centers for enhanced hydrogen evolution in alkaline solution, Angew. Chem. 132 (2020) 9067–9075, https://doi.org/10.1002/ange.201908760.

[60] N.N. Sun, D.Y. Zhou, W.W. Liu, S.Y. Shi, Z.J. Tian, F. Liu, S.D. Li, J.J. Wang, F. Ali, Tailoring surface chemistry and morphology of titanium nitride electrode for on-chip supercapacitors, ACS Sustain. Chem. Eng. 8 (2020) 7869–7878, https://doi.org/10.1021/acssuschemeng.0c00977.

[61] B. Yao, M.M. Li, J. Zhang, L. Zhang, Y. Song, W. Xiao, A. Cruz, Y.X. Tong, Y. Li, TiN paper for ultrafast-charging supercapacitors, Nano-Micro Lett. 12 (2020) 1–13, https://doi.org/10.1007/s40820-019-0340-7.

[62] P. Qin, X.X. Li, B. Gao, J.J. Fu, L. Xia, X.M. Zhang, K.F. Huo, W.L. Shen, P.K. Chu, Hierarchical TiN nanoparticles-assembled nanopillars for flexible supercapacitors with high volumetric capacitance, Nanoscale 10 (2018) 8728–8734, https://doi.org/10.1039/c8nr01485j.

[63] J.Y. Wang, F.X. Zhang, Z. Xu, W. Hu, H.H. Jiang, L.B. Liu, L.G. Gai, Gallium oxynitride@carbon cloth with impressive electrochemical performance for supercapacitors, Chem. Eng. J. 411 (2021) 128481, https://doi.org/10.1016/j.cej.2021.128481.

[64] Z.Q. Wu, B.B. Yang, H. Li, H.Y. Tong, X. Wang, H. Li, C.D. Li, L.L. Zhu, R.H. Wei, L. Hu, C.H. Liang, X.B. Zhu, Y.P. Sun, Solution-processable hierarchical-porous vanadium nitride films on silicon substrates for highly efficient symmetric supercapacitors, J. Power Sources 507 (2021) 230269, https://doi.org/10.1016/j.jpowsour.2021.230269.

[65] A. Salman, S.P. Sasikala, I.H. Kim, J.T. Kim, G.S. Lee, J.G. Kim, S.O. Kim, Tungsten nitride-coated graphene fibers for high-performance wearable supercapacitors, Nanoscale 12 (2020) 20239–20249, https://doi.org/10.1039/D0NR06636B.

[66] D. Mandal, J.Y. Jeong, B.S. Singu, S. Lee, W.J. Mun, H. Kim, Flexible all solid-state niobium nitride//activated carbon lithium-ion hybrid capacitor with high volumetric power and energy densities, J. Energy Storage 48 (2022) 104031, https://doi.org/10.1016/j.est.2022.104031.

WILEY-VCH

Supplementary Materials

2D Nonlayered Titanium Oxynitrides Intercalated with Nitrogen-Doped Graphene for Pseudocapacitive Energy Storage

Xiuli Li [a, c], Rui Huo [b], Zihuan Tang [a], Yulei Ren [a], Hao Song [a, *], Paul K Chu [d], Kaifu Huo [c, *]

[a] State Key Laboratory of Advanced Refractories, Institute of Advanced Materials and Nanotechnology, Wuhan University of Science and Technology, Wuhan 430081, China,

[b] School of Materials Science and Engineering, Central South University, Changsha 410083, China

[c] Wuhan National Laboratory for Optoelectronics (WNLO), School of Optical and Electronic Information, Huazhong University of Science and Technology, Wuhan 430074, China

[d] Department of Physics, Department of Materials Science and Engineering, and Department of Biomedical Engineering, City University of Hong Kong, Kowloon, Hong Kong 999077, China

* Corresponding authors

E-mail address: songhao201809@wust.edu.cn (H. Song); kfhuo@hust.edu.cn (K. F. Huo)

1. Samples Synthesis

1.1. Synthesis of the $K_{0.8}Ni_{0.4}Ti_{1.6}O_4$ (KNTO) and $H_{0.8}Ni_{0.4}Ti_{1.6}O_4 \cdot H_2O$ (HNTOH) nanosheets

All the chemical reagents were analytical grade and used as received without any additional purification. The 2D layered KNTO with an average size of 10 μm was produced by a modified molten salt method [1]. Typically, 1.38 g of anatase TiO_2 (Macklin, 99.8%), 0.73 g of NiO (Aladdin, 99.0%), and 3.20 g of K_2CO_3 (Aladdin, 99.0%) were mixed in a mortar for 1 h and then transferred to a muffle furnace which was heated to 1100 °C for 12 h in air to prepare the 2D layered KNTO nanosheets. The resulting KNTO nanosheets were further converted into HNTOH nanosheets via a hydrogen ion exchange process in diluted HNO_3 (1.0 M).

1.2. Intercalation of 1,8-diaminooctane into layered HNTOH

In a typical synthesis, 0.10 g of HNTOH, 0.09 g of 1,8-diaminooctane (DOE) and 10 g of H_2O were mixed under room temperature for 24 h and stirred to obtain the uniform suspension. The DOE molecules were intercalated into HNTOH layers due to the electrostatic interaction between positively-charged protonated DOE and negatively-charged $[Ni_{0.4}Ti_{1.6}O_4]^{0.8-}$ to produce HNTOH/DOE nanosheets by filtration and washing with water.

1.3. Synthesis of accordion-like TiN_xO_{1-x}/NG nanosheets, TiO_2/NG nanosheets and TiN_xO_{1-x} nanosheets

The accordion-like TiN_xO_{1-x}/NG nanosheets were synthesized by thermal nitriding of accordion-like HNTOH/DOE multilayered nanosheets at 750 ℃ under NH_3 atmosphere, followed by removal of Ni in diluted HCl. In a typical synthesis, the as-resulting 10g HNTOH/DOE was placed in a tube furnace, which was heated to 750 ℃ under NH_3 with the fux. The N and O contents were controlled by the annealing time (1, 3, 5, and 7 h) and the products were marked as N-TiO_2/NG, TiN_xO_{1-x}/NG-3, TiN_xO_{1-x}/NG-5, and TiN_xO_{1-x}/NG-7, respectively.

For comparison, the pure TiN_xO_{1-x} nanosheets were prepared by nitriding the HNTOH nanosheets with a similar process and the TiO_2/NG nanosheets were obtained by annealing the HNTOH/DOE nanosheets at 750 ℃ for 5 h under Ar atmosphere.

2. Morphology, Structure and Composition Characterizations

The morphology of the products was examined by scanning electron microscopy (SEM, ThermoFisher/Apreo S HiVac) and transmission electron microscopy (TEM, CF-HR/JEM-F200). X-ray diffraction (XRD, Rigaku/SmartLab) with Cu Kα radiation (λ=1.5405 Å), Raman spectra under laser excitation at 532 nm (LabRAM HR Evolution) and X-ray photoelectron spectrometer (XPS, AXIS SUPRA+) with Al Kα radiation in twin anode were used to measure the crystal structure and composition of samples. The specific surface area of samples was measured by the automatic gas adsorption analyzer (BET, Autosorb-iQ) at 77 K. TG measurement was carried out by Discovery SDT 650 thermal analyzer. XANES measurements were performed at 1W1B station in Beijing Synchrotron Radiation Facility (BSRF). XANES were set-up with a fast-scanning silicon (111) double-crystal monochromator. XANES data was processed using Athena software of the Demeter package.

3. Electrochemical Measurements

All electrochemical measurements were conducted via a PMC-200 electrochemical workstation. The capacitive properties were assessed using a three-electrode configuration with the Ag/AgCl (1.0 M KCl) and platinum foil as the reference and counter electrodes. The working electrode was fabricated by mixing the slurry containing the as-prepared samples, acetylene black, and polytetrafluoroethylenes (PTFE) with 8:1:1 weight ratio in absolute ethyl alcohol. The resulting homogeneous slurry was casted onto the titanium mesh (200 mesh) with a pressure of 20 MPa to form film electrodes with 1 cm × 1 cm in size. The cyclic voltammetry (CV) was tested at the sweep rate of 20 mV s^{-1} in 0.5 M H_2SO_4 (0.0 ~ 0.8 V vs. Ag/AgCl). The

galvanostatic charge/discharge (GCD) measurements were performed at different volume current densities from 1 to 20 A cm^{-3}. To determine which ions specifically contribute to the redox reactions involved in pseudcapacitive charge storage processes, H^+ and SO_4^{2-} ions were isolated by coupling them with the inactive counter $(C_2H_5)_4N^+$ and BF_4^- ions because they are recognized as non-reactive towards nitrides in redox reactions. Therefore, the ion isolation experiments of TiN_xO_{1-x}/NG were carried out by CV scanning and GCD tests in 0.5 M H_2SO_4, 0.5 M $[(C_2H_5)_4N]_2SO_4$, 1.0 M $[(C_2H_5)_4N]BF_4$, and 1.0 M HBF_4 aqueous electrolytes at room temperature. The electrochemical impedance spectroscopy (EIS) was acquired at a frequency range between 100 kHz and 10 mHz with an amplitude voltage of 5 mV. The volumetric specific capacitances C_V (F cm^{-3}) were calculated according to the following equations:

$$C_V=(I\times\Delta t)/(\Delta V\times V) \quad (1)$$

Among them, C_V (F cm^{-3}) is the volumetric specific capacitance, I (A) is the current, Δt (s) designates the discharge time, V (cm^3) denotes the volume of the TiN_xO_{1-x}/NG electrode, and ΔV (V) is the voltage window.

The all-solid-state symmetrical device was fabricated by divided two similar electrodes by H_2SO_4/PVA gel electrolyte. The preparation of H_2SO_4/PVA electrolyte was described in our previous paper [2]. The total volumetric capacitance (C_{Cell}, F cm^{-3}), volumetric energy density (E, Wh cm^{-3}), and power density (P, W cm^{-3}) were obtained by the following equations:

$$C_{Cell}=(I\times\Delta t)/(\Delta V\times V) \quad (2)$$

$$E=0.5C_{Cell}\times\Delta V^2/3600 \quad (3)$$

$$P=E\times3600/\Delta t \quad (4)$$

where V_{Cell} (cm^3) is the total volume of both positive and negative electrodes, ΔV (V) is the potential range, Δt (s) is the discharge time.

4. *In Situ* Electrochemical Spectroscopy Characterization

4.1. In situ electrochemical Raman spectroscopy

To monitor the redox processes of the electrode, *in situ* Raman measurement was performed using a LabRAM HR evolution system by applying a 532 nm excitation wavelength. The Raman spectroscopy data of the electrode were collected one by one via mapping mode accompanied by CV measurement at 1 mV s^{-1} in a three-electrode electrochemical flow cell (GaossUnion Technology Co., Ltd., Wuhan, China) with a Pt wire counter electrode and an Ag/AgCl (1.0 M KCl) reference electrode. The working electrodes were prepared by coating the slurry based on 8:1:1 weight ratio of TiN_xO_{1-x}/NG-5, carbon black, and PTFE on the carbon paper. The spectrum acquisition time of 30 s was used to obtain the Raman signals with a good signal-to-noise ratio. The applied exploration time was 10 s with two sweeps per spectrum, and the spectrum acquisition interval was 100 s.

4.2. In situ ATR FT-IR spectroscopy

The *in situ* attenuated total reflectance Fourier-transform infrared (ATR FT-IR) studies were performed using three-electrode system similar to the *in situ* Raman test, which was conducted using a FT-IR spectrometer (Nicolet 6700, Thermo-Fisher Scientific) with an extended range diamond ATR accessory (Shanghai Linglu Instrument Co. Ltd). All FT-IR spectra data were collected using a liquid nitrogen cooled HgCrTe (MCT/A) detector over 650 ~ 4000 cm^{-1} at a resolution of 4 cm^{-1}. Each spectrum was obtained with 32 scans, and the spectrum acquisition interval was set at 100 s.

4.3. Electrochemical quartz crystal microbalance (EQCM) measurement

The EQCM system combined with a PMC-200 electrochemical workstation were applied for real-time monitoring the mass change of the electrode. The EQCM tests employed a gold-coated quartz crystal as the working electrode, on which the active material coating was prepared by drip-coating the slurry of the TiN_xO_{1-x}/NG-5, acetylene black, and PTFE with a mass ratio of 8:1:1. An Ag/AgCl (1.0 M KCl) electrode and a Pt wire were applied as the reference and counter electrodes, respectively. The resonance frequency was recorded

simultaneously with the CV scanning at the sweep rate of 10 mV s^{-1} in 0.5 M H_2SO_4 (0.0 ~ 0.8 V vs. Ag/AgCl) using the quartz crystal microbalance (QCM922) in combination with a VersaSTAT 3 Potentiostat/Galvanostat. The shift of the resonance frequency of the quartz resonator (Δf) can be converted into a mass change (Δm, μg) of the gold-coated quartz crystal electrode by applying the Sauerbrey's equation:

$$\Delta m=-(\Delta f\times A\times\sqrt{\mu\rho})/2f_0^2 \quad (5)$$

where A is the active crystal surface (0.198 cm^2), ρ is the density of quartz (2.65 g cm^{-3}), μ is the shear modulus of quartz (2.947 × 10^{11} g cm^{-1} × s^{-2}) and f_0 is the reference frequency of the quartz crystal (9.00 MHz). According to this equation, the change of 1 Hz equals 1.068 ng.

5. DFT Calculations

The density functional theory (DFT) calculations were performed based on the HR-TEM results using the (200) facet of TiN_xO_{1-x}, where the value of x was 0.5 according to the XPS results. The Vienna Ab initio Simulation Package (VASP) with exchange-correlation functional of gradient approximation (GGA) was applied to perform the DFT calculations using the Perdew-Burke-Ernzerhof (PBE) formulation [3-5]. The projected augmented wave (PAW) potentials were chosen to describe the ionic cores and take valence electrons into account using a plane wave basis set with a kinetic energy cutoff of 450 eV [6,7]. A grid of 1 × 1 × 1 Monkhorst-Pack k-points was used for the structural relaxation. The force convergence criterion and energy were set to −0.05 eV $Å^{-1}$ and 1 × 10^{-5} eV for the structural optimization. The 15 Å vacuum layer was normally added to the surface to eliminate artificial interactions between periodic images. Spin polarization method was adopted to describe the magnetic system. The adsorption energy of H^+ adsorbed on optimized $TiN_{0.5}O_{0.5}$ (200) slab model was calculated via the following equation:

$$\Delta E_{(H^+)^*}=E_{(H^+)^*}-(E_{surf}+E_{H^+}) \quad (6)$$

Where $E_{(H^+)^*}$, E_{surf} and E_{H^+} represent the total energy of H^+ adsorbed on the $TiN_{0.5}O_{0.5}$ (200) slabs, the total energy of the clean $TiN_{0.5}O_{0.5}$ (200) slab as well as the energy of H^+ in its bulk structure.

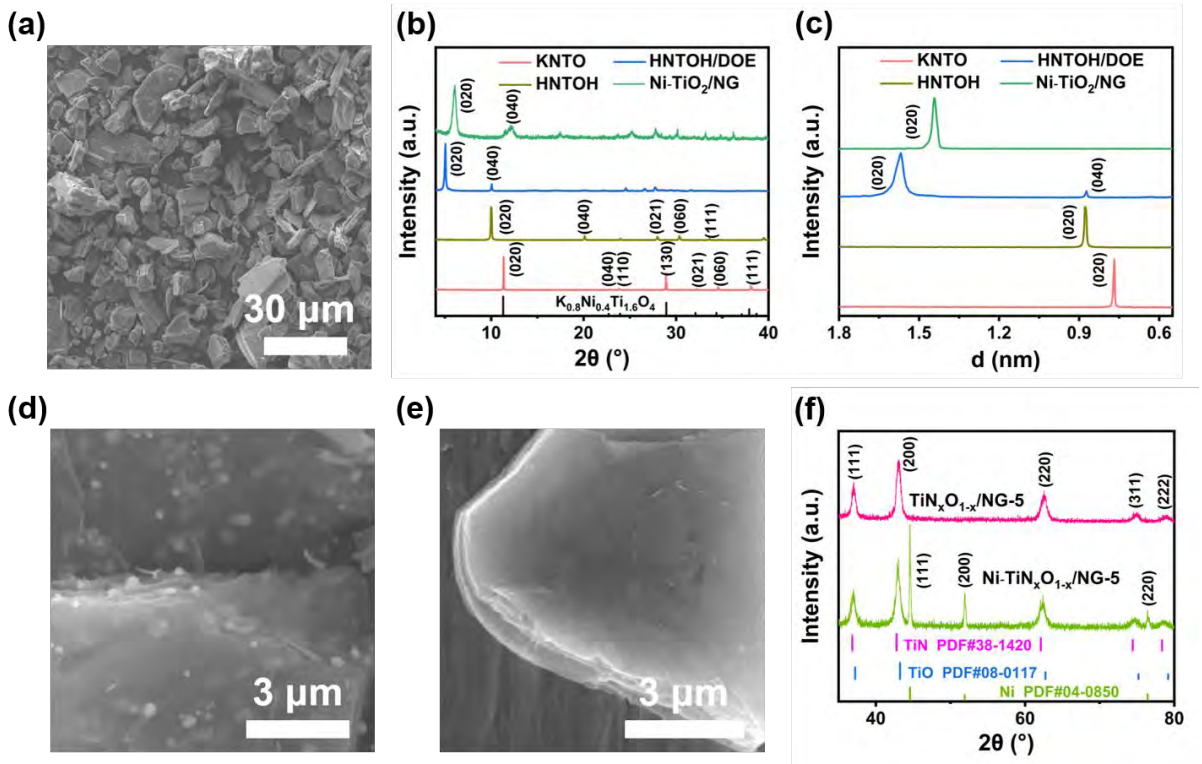

Fig. S1. (a) SEM image of KNTO; (b) XRD patterns and (c) small-angle XRD patterns with the interlayer spacing of KNTO, HNTOH, HNTOH/DOE and Ni-TiO_2/NG; SEM image of (d) Ni-TiN_xO_{1-x}/NG-5 and (e) TiN_xO_{1-x}/NG-5; (f) XRD patterns of the Ni-TiN_xO_{1-x}/NG-5 and TiN_xO_{1-x}/NG-5.

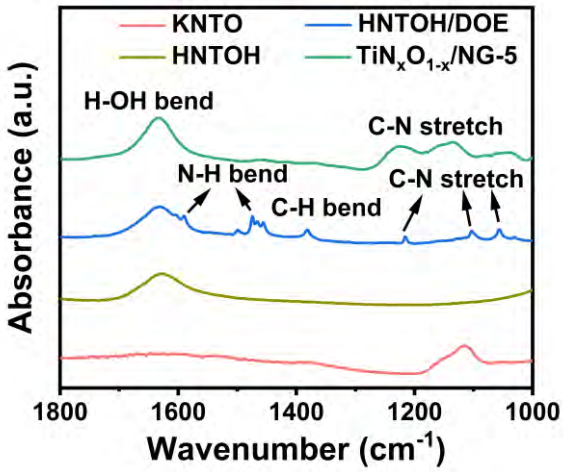

Fig. S2 IR spectra of KNTO, HNTOH, HNTOH/DOE and TiN_xO_{1-x}/NG-5;

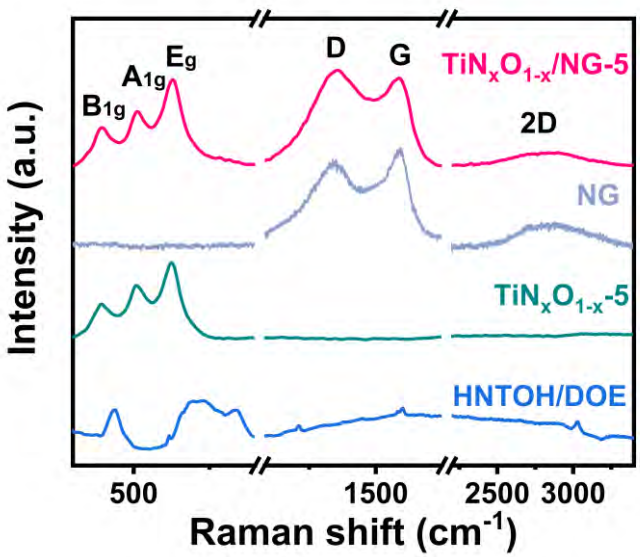

Fig. S3. Raman spectra of the HNTOH/DOE, TiN_xO_{1-x}-5, NG and TiN_xO_{1-x}/NG-5.

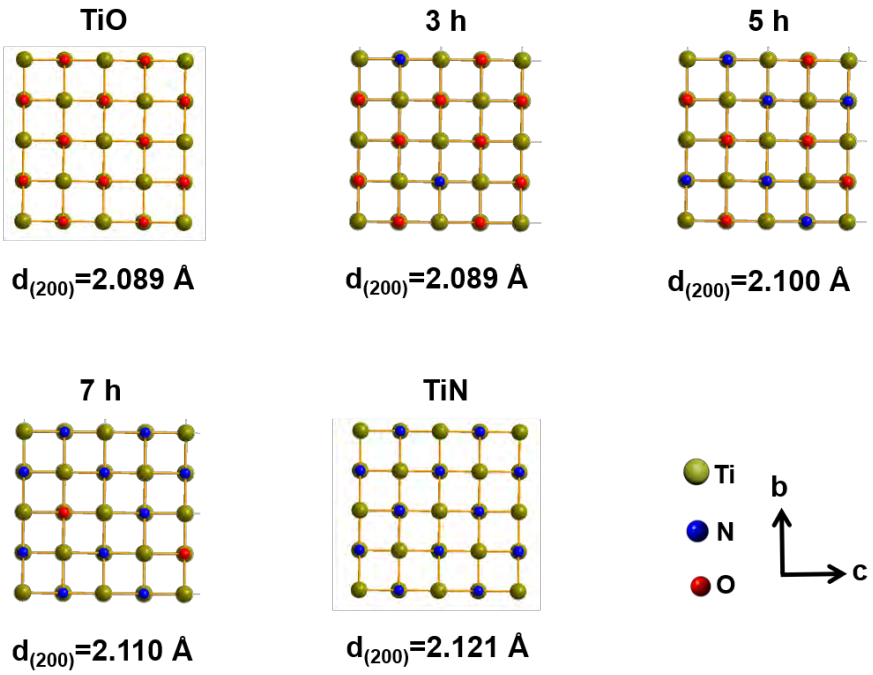

Fig. S4. The crystal lattice distances of TiO, TiN, and TiN_xO_{1-x} in TiN_xO_{1-x}/NG with different nitridation times.

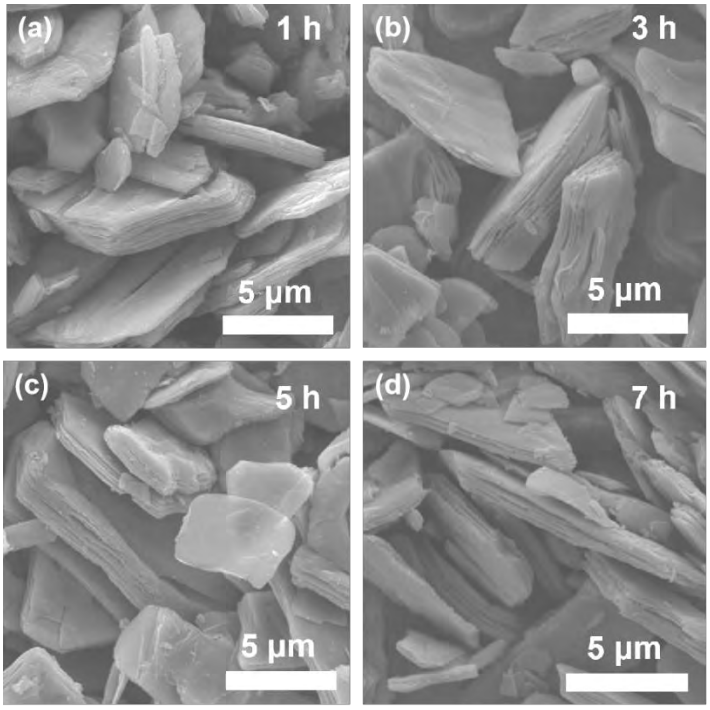

Fig. S5. SEM images of (a) N-TiO_2/NG, (b) TiN_xO_{1-x}/NG-3, (c) TiN_xO_{1-x}/NG-5, and (d) TiN_xO_{1-x}/NG-7.

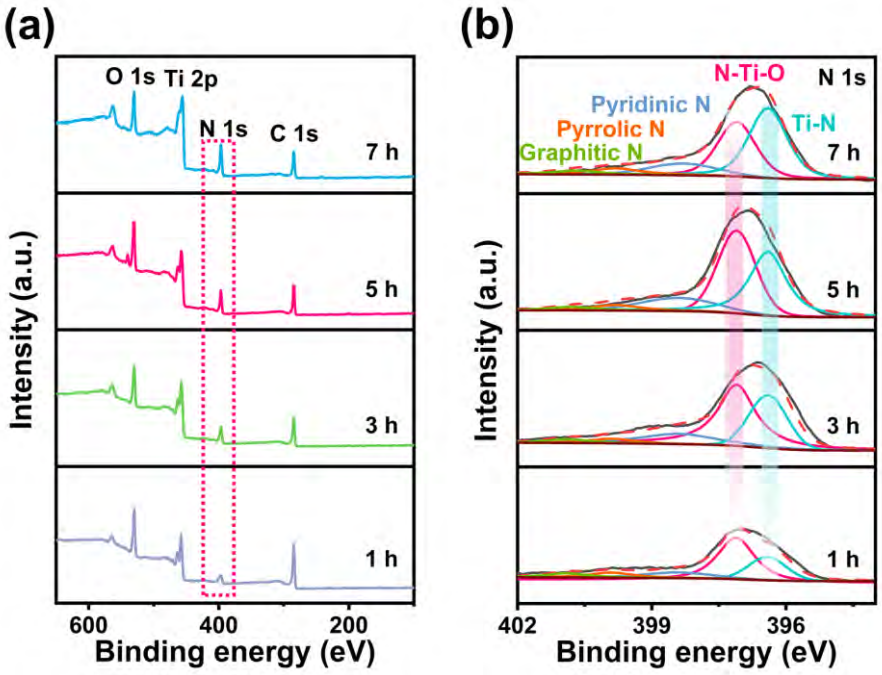

Fig. S6. (a) Full XPS spectra and (b) N 1*s* XPS spectra of N-TiO_2/NG, TiN_xO_{1-x}/NG-3, TiN_xO_{1-x}/NG-5, and TiN_xO_{1-x}/NG-7.

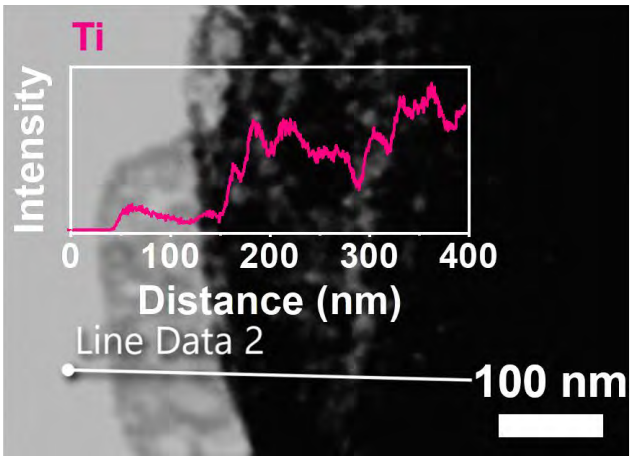

Fig. S7. The STEM-EDS image of TiN_xO_{1-x}/NG-5.

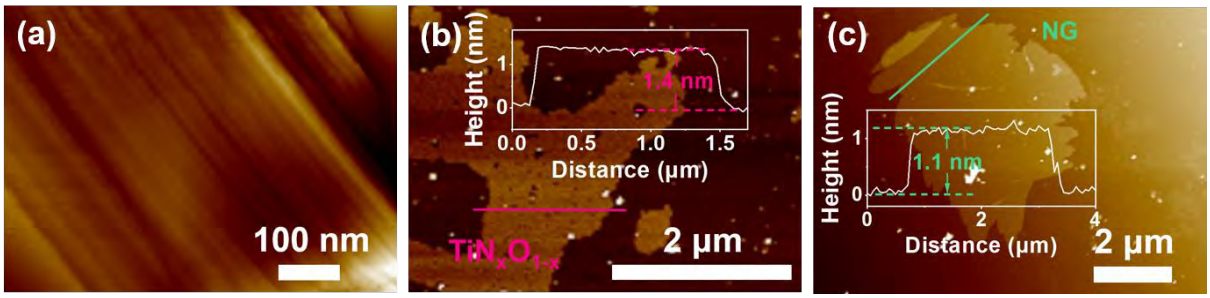

Fig. S8. AFM images of (a) TiN_xO_{1-x}/NG-5, (b) TiN_xO_{1-x} and (c) NG.

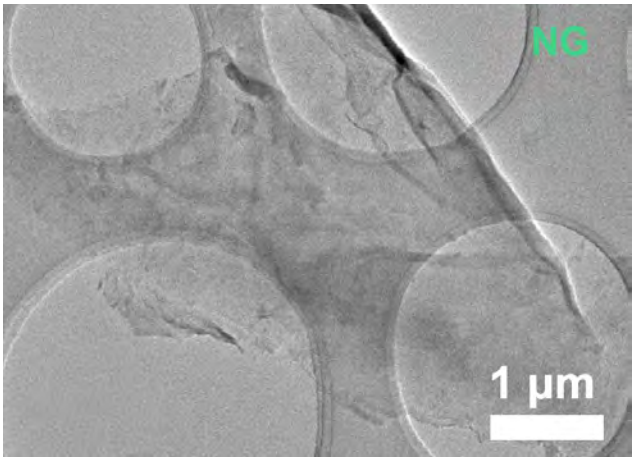

Fig. S9. The TEM image of individual NG nanosheets.

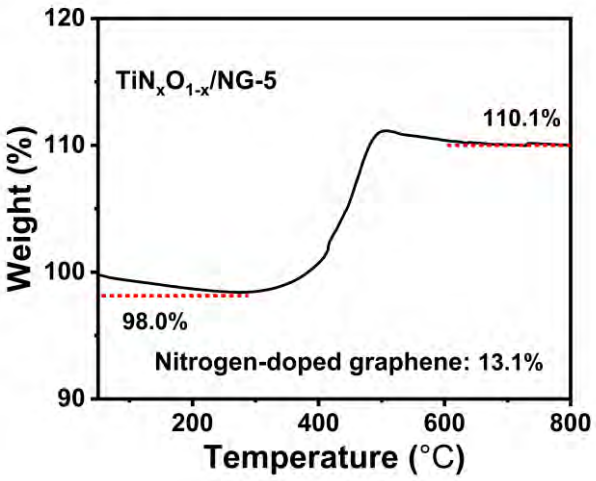

Fig. S10. Thermogravimetric analysis plots of TiN_xO_{1-x}/NG-5.

The ratio of TiN_xO_{1-x} and nitrogen-doped graphene in the TiN_xO_{1-x}/NG-5 can be calculated by the weight increment in the temperature range from 200 ℃ to 600 ℃, where the TiN_xO_{1-x} are converted into TiO_2 along with the oxidation of the NG. **Fig. S10** is the TG curve of TiN_xO_{1-x}/NG-5 under Air. The 2% weight loss before 200 °C represents adsorbing water and the mass is increased from 98% to 110.1% after oxidation. During this process, the carbon oxide gases are released and the TiN_xO_{1-x}/NG-5 is finally transformed into solid TiO_2, leading to the mass increasing. The N/O ratio of TiN_xO_{1-x}-5h is measured to be 1/1 according to the XPS results in **Fig. S6**, so we could calculate the NG content within TiN_xO_{1-x}/NG-5 ($TiN_{0.5}O_{0.5}$/NG) by the following equation based on the same Ti molar ratio of TiN_xO_{1-x}/NG-5 and TiO_2 product:

$$98\% \times (1\text{-NG}\%)/M(TiN_{0.5}O_{0.5}) = 110.1\%/M(TiO_2)$$

Given that $M(TiN_{0.5}O_{0.5})$ = 62.87 g mol^{-1} and $M(TiO_2)$ = 79.9 g mol^{-1}, the NG content is calculated to be 11.6 wt%.

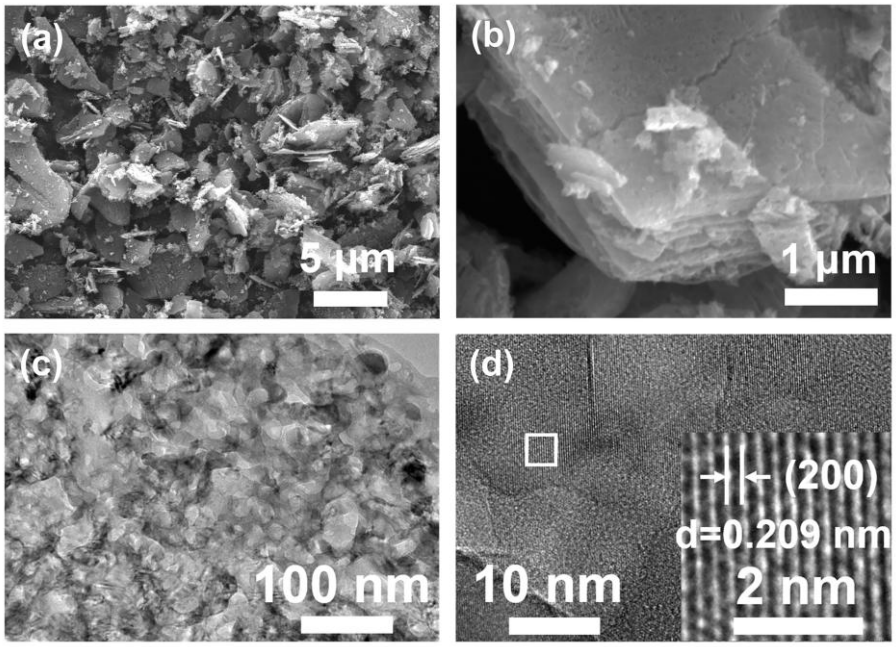

Fig. S11. (a, b) SEM images and (c, d) TEM images of TiN_xO_{1-x}-5.

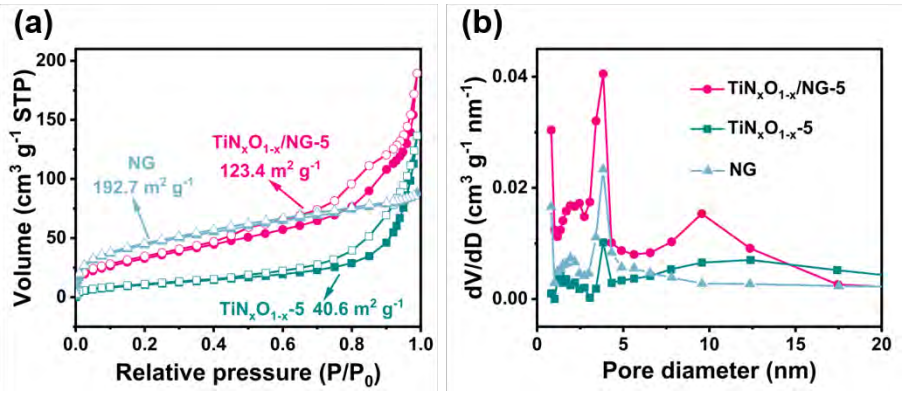

Fig. S12. (a) The nitrogen adsorption-desorption isotherm and (b) pore size distribution curves of TiN_xO_{1-x}-5 and TiN_xO_{1-x}/NG-5.

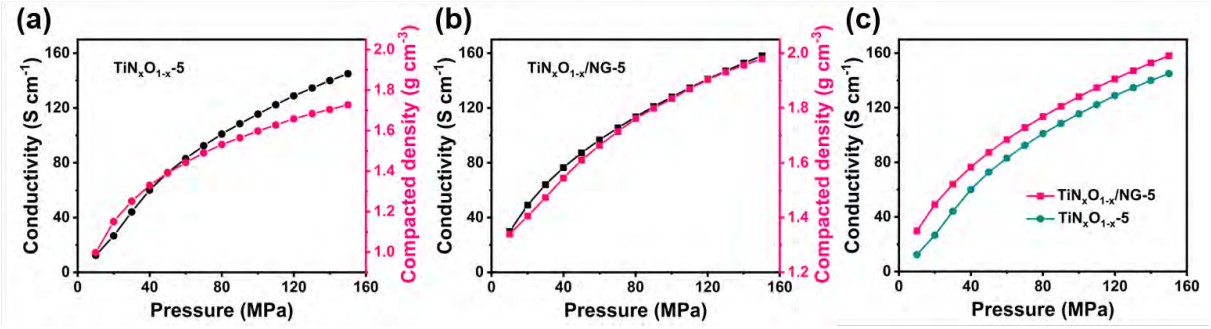

Fig. S13. (a, b) The conductivity and compaction density variations with pressure of TiN_xO_{1-x}-5 and TiN_xO_{1-x}/NG-5; (c) Conductivity variations with pressure for TiN_xO_{1-x}-5 and TiN_xO_{1-x}/NG-5.

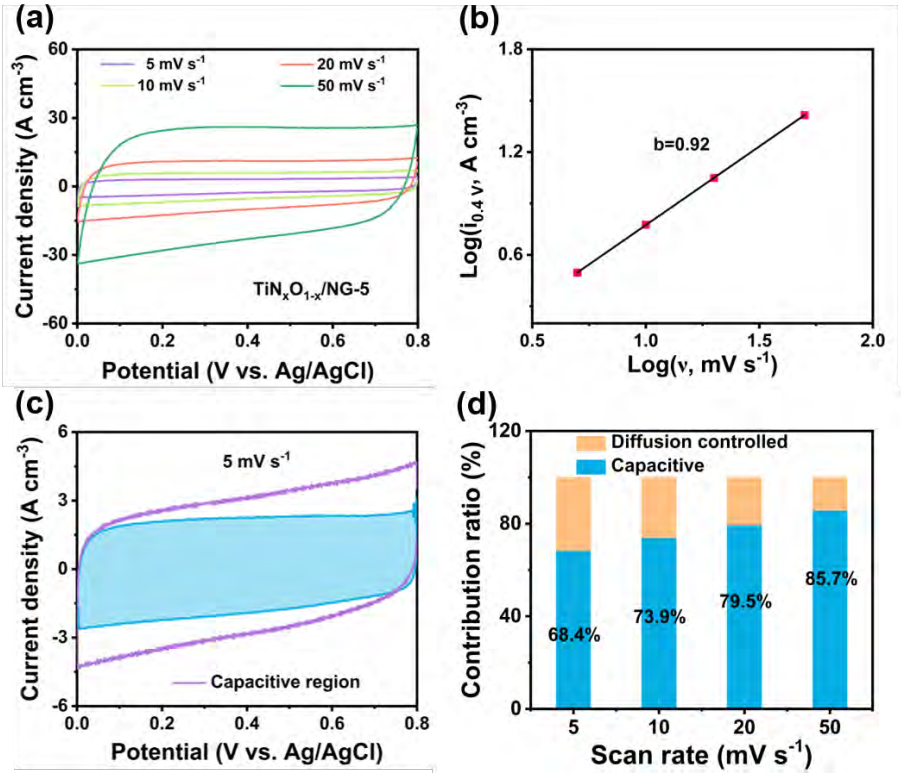

Fig. S14. (a) CV plots at scanning rates from 5 to 50 mV s^{-1}; (b) The plots of log (i) versus log (v) obtained at 0.4 V; (c) Capacitive contribution to the charge storage at a scan rate of 5 mV s^{-1}; (d) The proportion of capacitive contribution at different scan rates.

In a cyclic voltammetry experiment, the timescale of the experiment is controlled by the sweep rate (v, mV s^{-1}). The current response to an applied sweep rate will vary depending on whether the redox reaction is diffusion-controlled or surface-controlled (capacitive). According to Dunn's method, the scan rate-response current relation should obey the law $i = av^b$, which can be converted to log (i) = $b$log (v) + log (a). A b-value of 0.5 typically corresponds to a diffusion-controlled process associated with a battery-like reaction, while a b-value of 1 indicates capacitive characteristics. For a redox reaction limited by semi-infinite linear diffusion, the current response varies with $v^{1/2}$; for a capacitive process, the current varies directly with v. Therefore, the equation $i = k_1v + k_2v^{1/2}$ is employed to quantitatively analyze the capacitive contribution at varying scan rates, where k_1v and $k_2v^{1/2}$ represent the contribution value of

capacitance behavior and diffusion behavior to the response current, respectively. Solving for the values of k_1 and k_2 at each potential allows for the separation of the diffusion and capacitive currents. Based on the CV plots of TiN_xO_{1-x}/NG at scanning rates from 5 to 50 mV s^{-1}, the *b*-value obtained by fitting the line of log (*i*) versus log (*v*) is 0.92, suggesting the fast capacitive process in TiN_xO_{1-x}/NG electrode. The proportion of the capacitive/capacity contribution in the total charge storage is 68.4% at a scan rate of 5 mV s^{-1}, implying the fast charge-transfer efficiency. Notably, the capacitive contribution for TiN_xO_{1-x}/NG monotonously rising from 68.4% to 85.7% with the scan rate increasing, confirming the charge-storage in TiN_xO_{1-x}/NG mainly originates from the surface capacitive behavior.

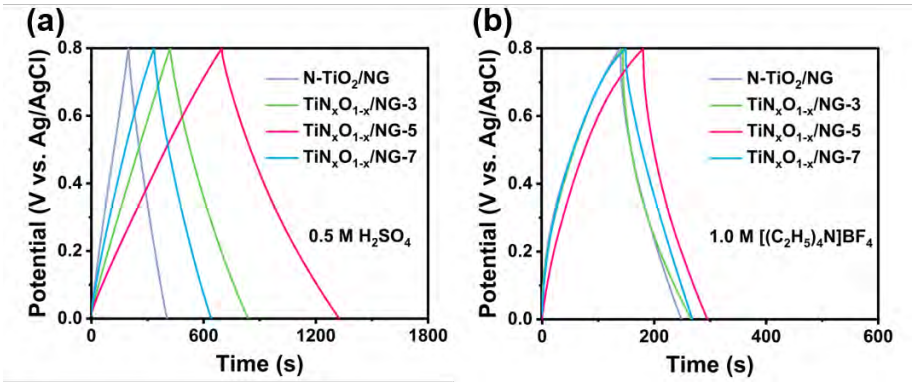

Fig. S15. The GCD curves of N-TiO_2/NG, TiN_xO_{1-x}/NG-3, TiN_xO_{1-x}/NG-5, and TiN_xO_{1-x}/NG-7 in (a) 0.5 M H_2SO_4 and (b) 1.0 M $[(C_2H_5)_4N]BF_4$ electrolytes at a current density of 1 A cm^{-3}.

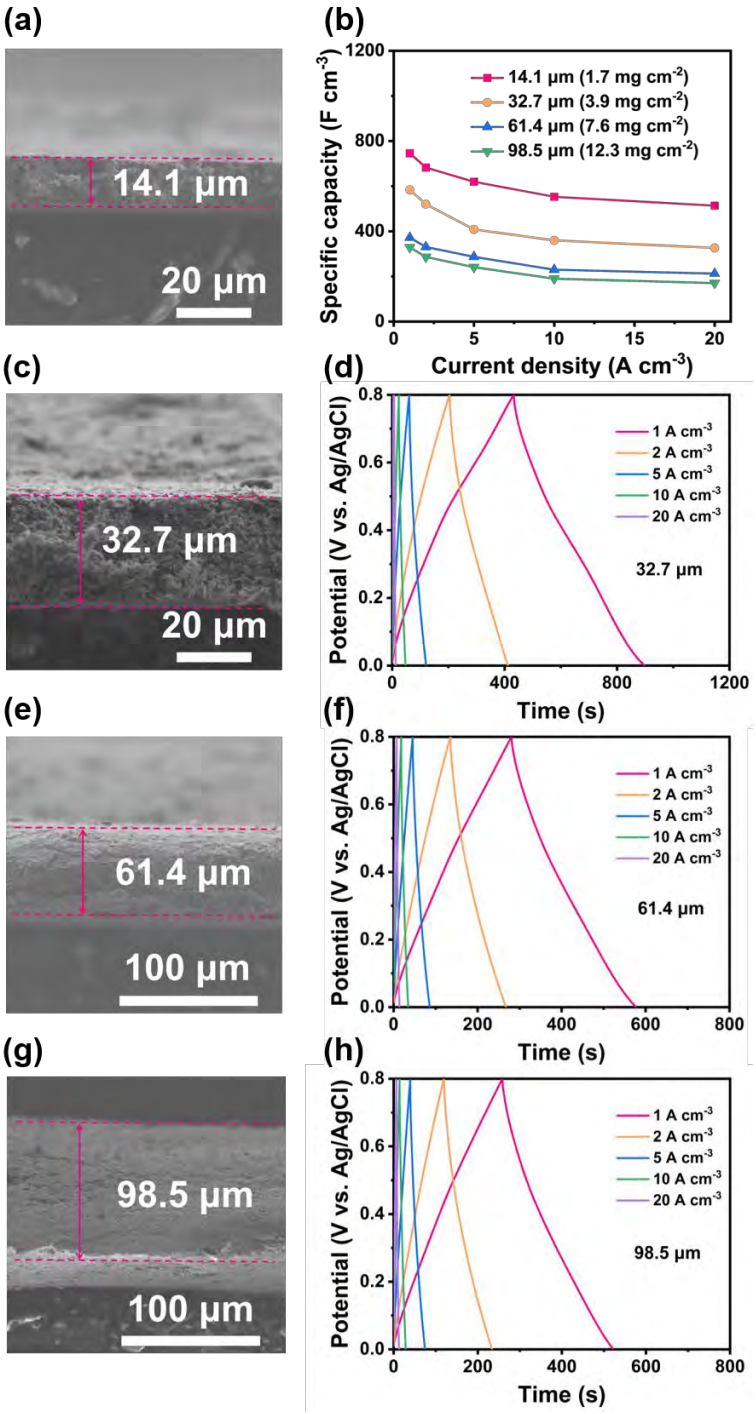

Fig. S16. (a) Side-view SEM image showing that the thickness (14.1 μm) of the TiN_xO_{1-x}/NG-5; (b) The volumetric capacitances of TiN_xO_{1-x}/NG-5 electrodes with the thicknesses of 14.1μm (1.7 mg cm^{-2}), 32.7 μm (3.9 mg cm^{-2}), 61.4 μm (7.6 mg cm^{-2}), and 98.5 μm (12.3 mg cm^{-2}) at different current densities; Side-view SEM images and GCD profiles of the TiN_xO_{1-x}/NG-5 electrode with a thickness of (c, d) 32.7, (e, f) 61.4 and (g, h) 98.5 μm.

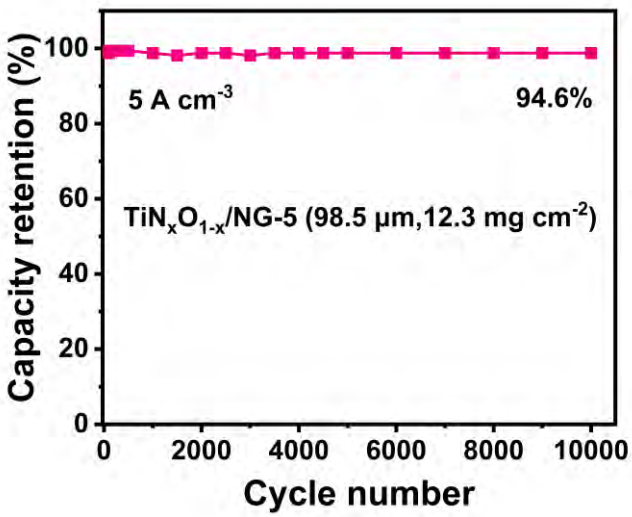

Fig. S17. Cycling stability of TiN_xO_{1-x}/NG-5 electrodes with 98.5 μm thickness (12.3 mg cm^{-2}) at a current density of 5 A cm^{-3}.

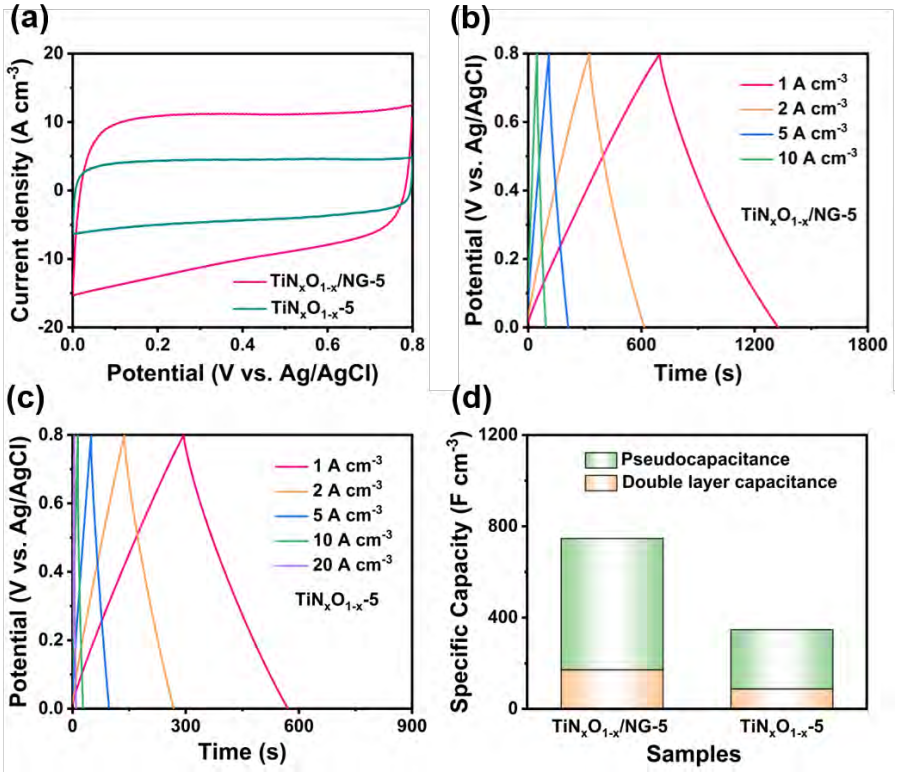

Fig. S18. (a) CV curves of TiN_xO_{1-x}/NG-5 and TiN_xO_{1-x}-5 at 20 mV s^{-1}; GCD curves of (b) TiN_xO_{1-x}/NG-5 and (c) TiN_xO_{1-x}-5 at different current densities in 0.5 M H_2SO_4 electrolytes; (d) Contribution of double layer capacitance and pseudocapacitance of TiN_xO_{1-x}-5 and TiN_xO_{1-x}/NG at 1 A cm^{-3}.

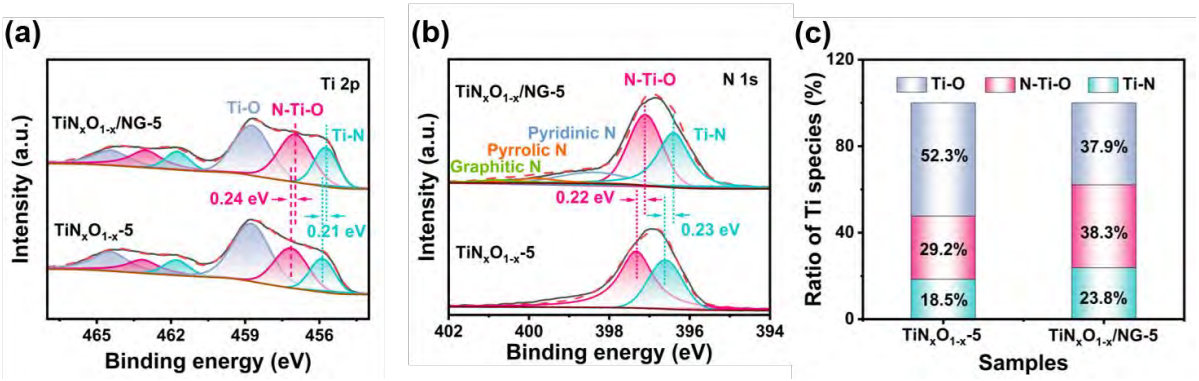

Fig. S19. (a) Ti 2*p* XPS spectra, (b) N 1*s* XPS spectra and (c) ratios of Ti species of the TiN_xO_{1-x}/NG-5 and TiN_xO_{1-x}-5.

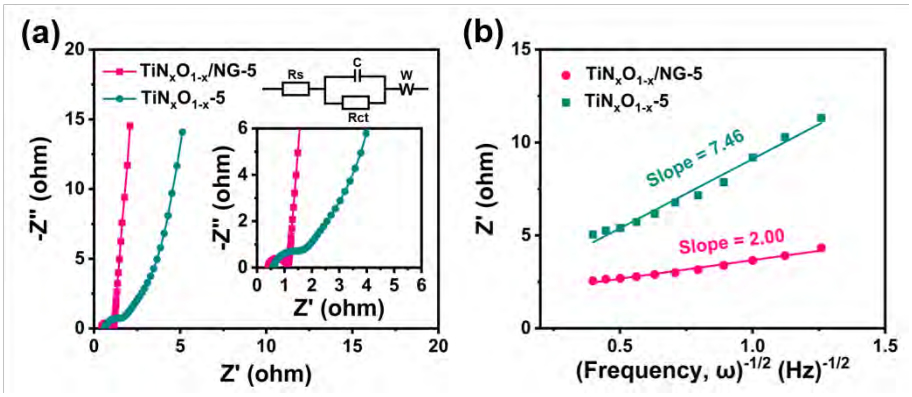

Fig. S20. (a) Nyquist plots and (b) Z' against $\omega^{-1/2}$ plots of the TiN_xO_{1-x}/NG-5 and TiN_xO_{1-x}-5.

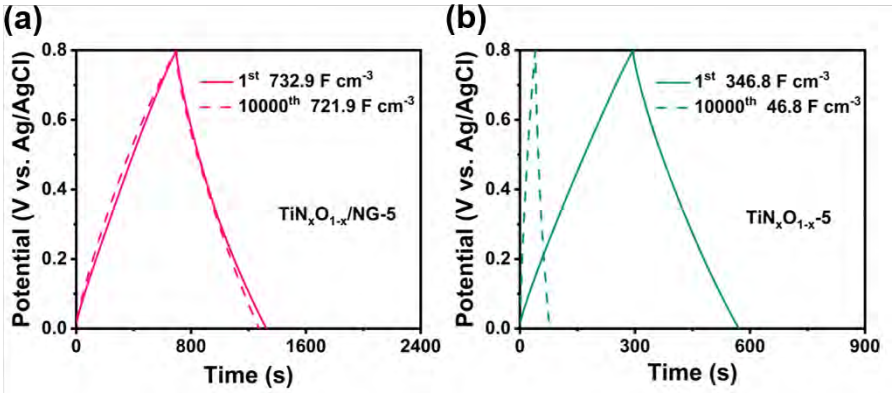

Fig. S21. The 1st and 10000th cycle GCD curves of (a) TiN_xO_{1-x}-5 and (b) TiN_xO_{1-x}/NG-5 electrodes in the 0.5 M H_2SO_4 electrolyte at a current density of 1 A cm^{-3}.

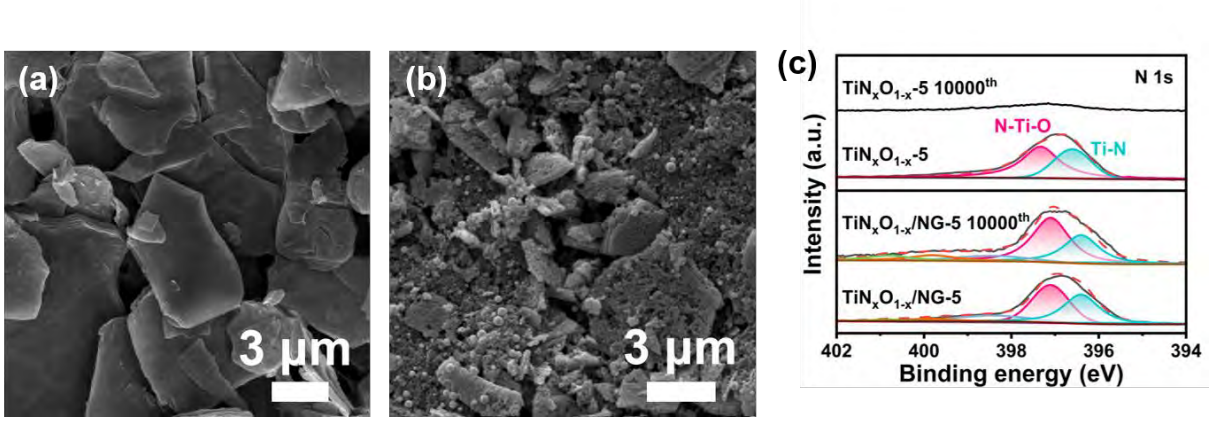

Fig. S22. SEM image of (a) TiN_xO_{1-x}/NG-5 and (b) TiN_xO_{1-x}-5 electrode after 10,000 cycles at 1 A cm^{-3}; (c) N 1*s* XPS spectra collected for TiN_xO_{1-x}/NG-5 and TiN_xO_{1-x}-5 electrodes before and after 10,000 cycles in 0.5 M H_2SO_4 electrolytes.

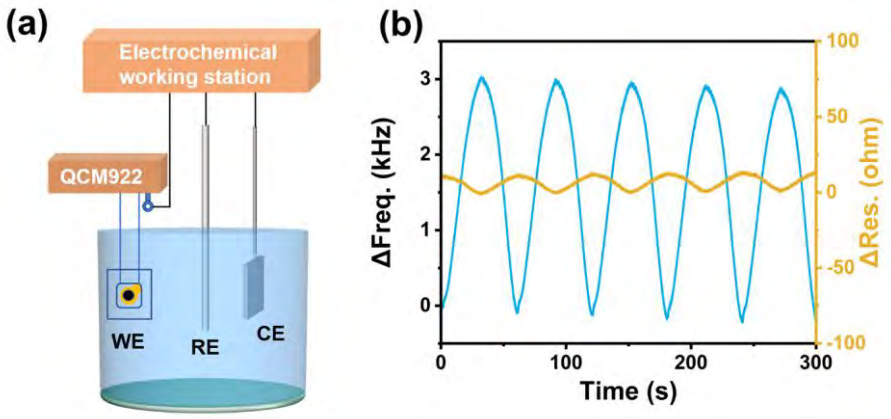

Fig. S23. (a) Schematic illustration of the electrochemical quartz crystal microbalance (EQCM) with three-electrode cell; (b) Raw EQCM data of TiN_xO_{1-x}/NG-5-coated quartz electrode in 0.5 M H_2SO_4 electrolytes.

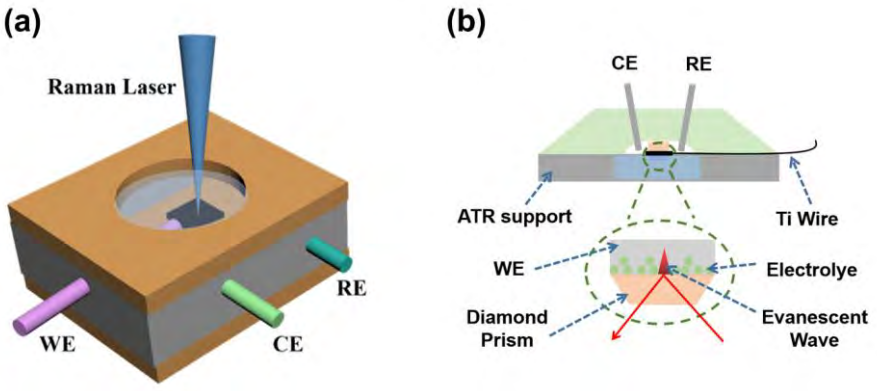

Fig. S24. Schematic diagram of the three-electrode cell for (a) *in situ* Raman scattering spectroscopy investigation and (b) *in situ* FTIR spectroscopy investigation.

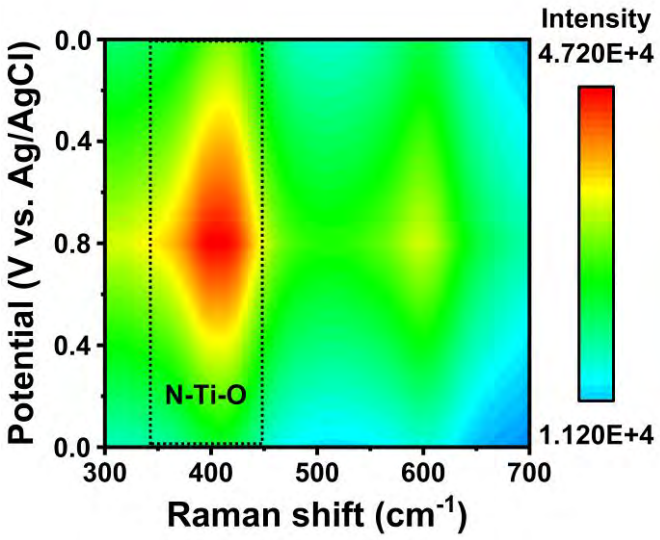

Fig. S25. Mapping mode of the Raman signal evolution of TiN_xO_{1-x}/NG-5 in 0.5 M H_2SO_4 electrolytes.

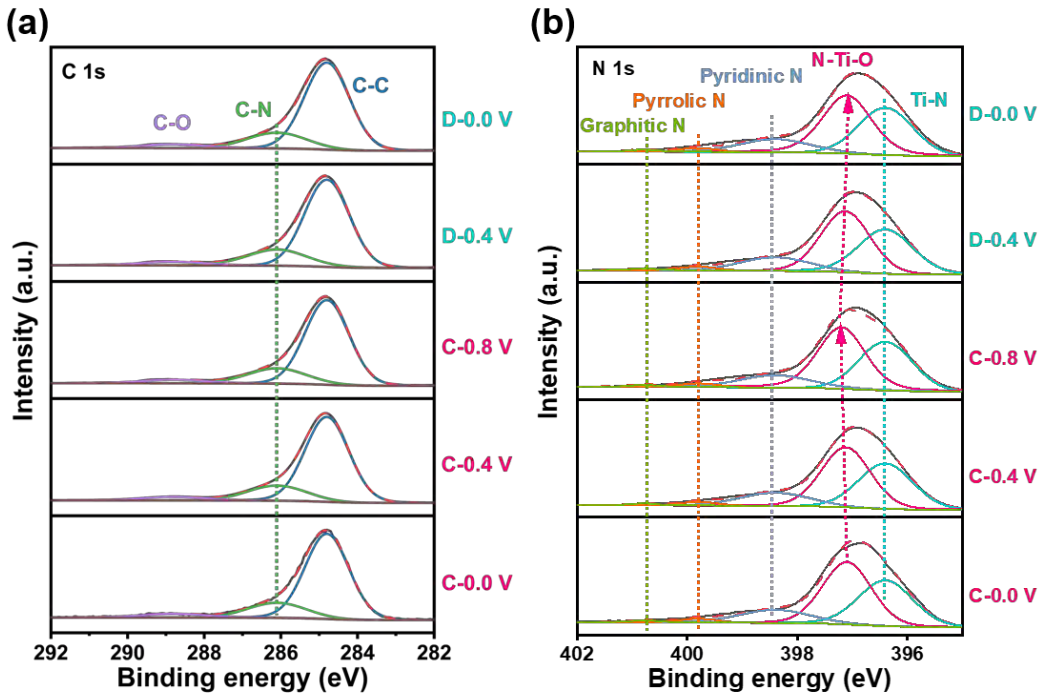

Fig. S26. *Ex situ* XPS (a) C 1*s* and (b) N 1*s* spectra of TiN_xO_{1-x}/NG-5 at different potentials during CV measurement at 1 mV s^{-1}.

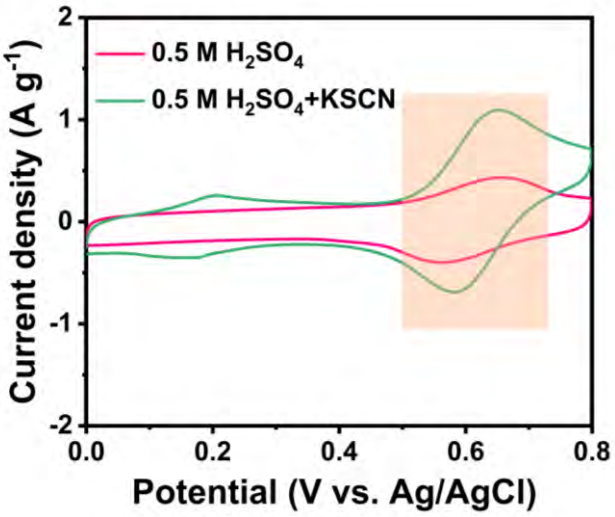

Fig. S27. CV curves of TiN_xO_{1-x}/NG-5 with and without the addition of 10 mM KSCN in 0.5 M H_2SO_4 electrolytes.

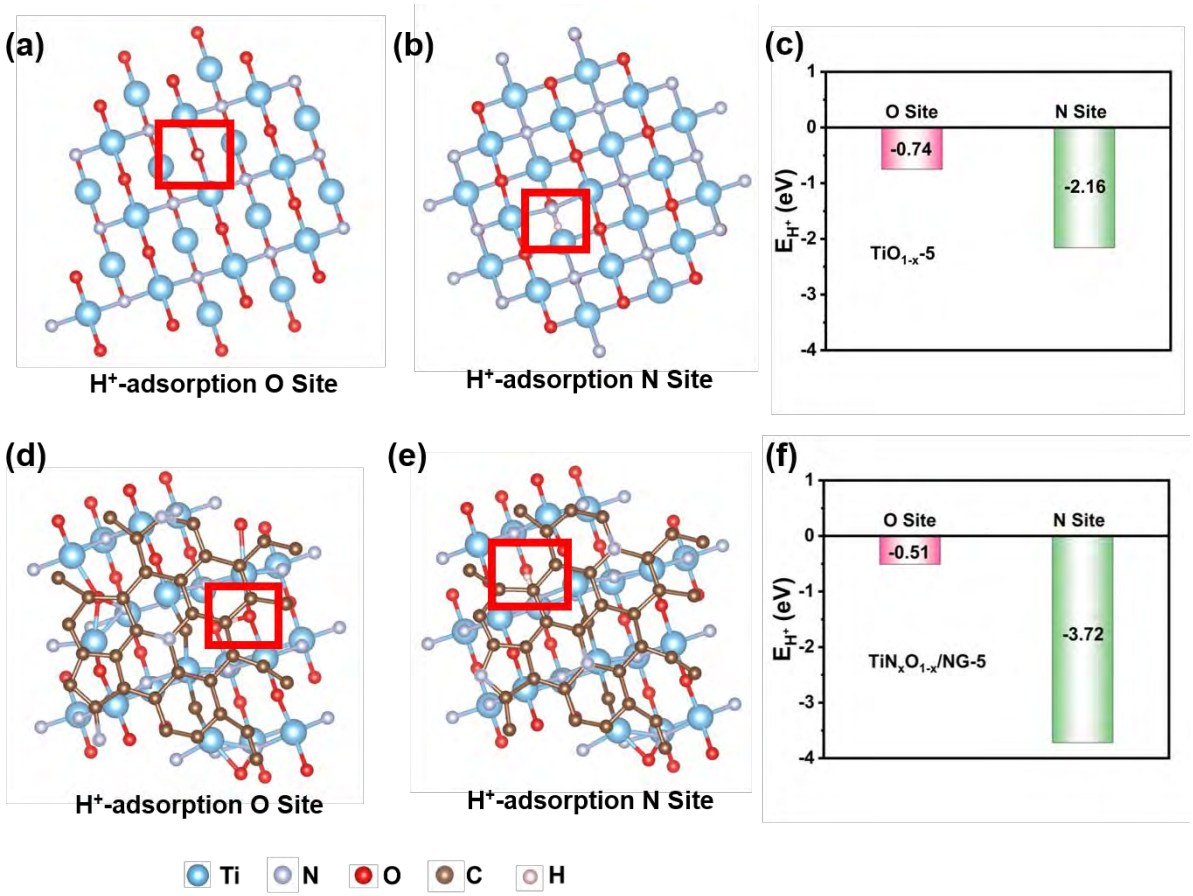

Fig. S28. The atomic configurations of hydrogen ion adsorption on the (200) plane of TiN_xO_{1-x}-5 at (a) O site and (b) N site; (c) Calculated H^+ adsorption energies of TiN_xO_{1-x}-5 at O sites and N sites; (d) The atomic configurations of hydrogen ion adsorption on the heterointerface between the (200) plane of TiN_xO_{1-x} and single-layered N-doped graphene at (d) O site and (e) N site; (f) Calculated H^+ adsorption energies of TiN_xO_{1-x}/NG-5 at O sites and N sites.

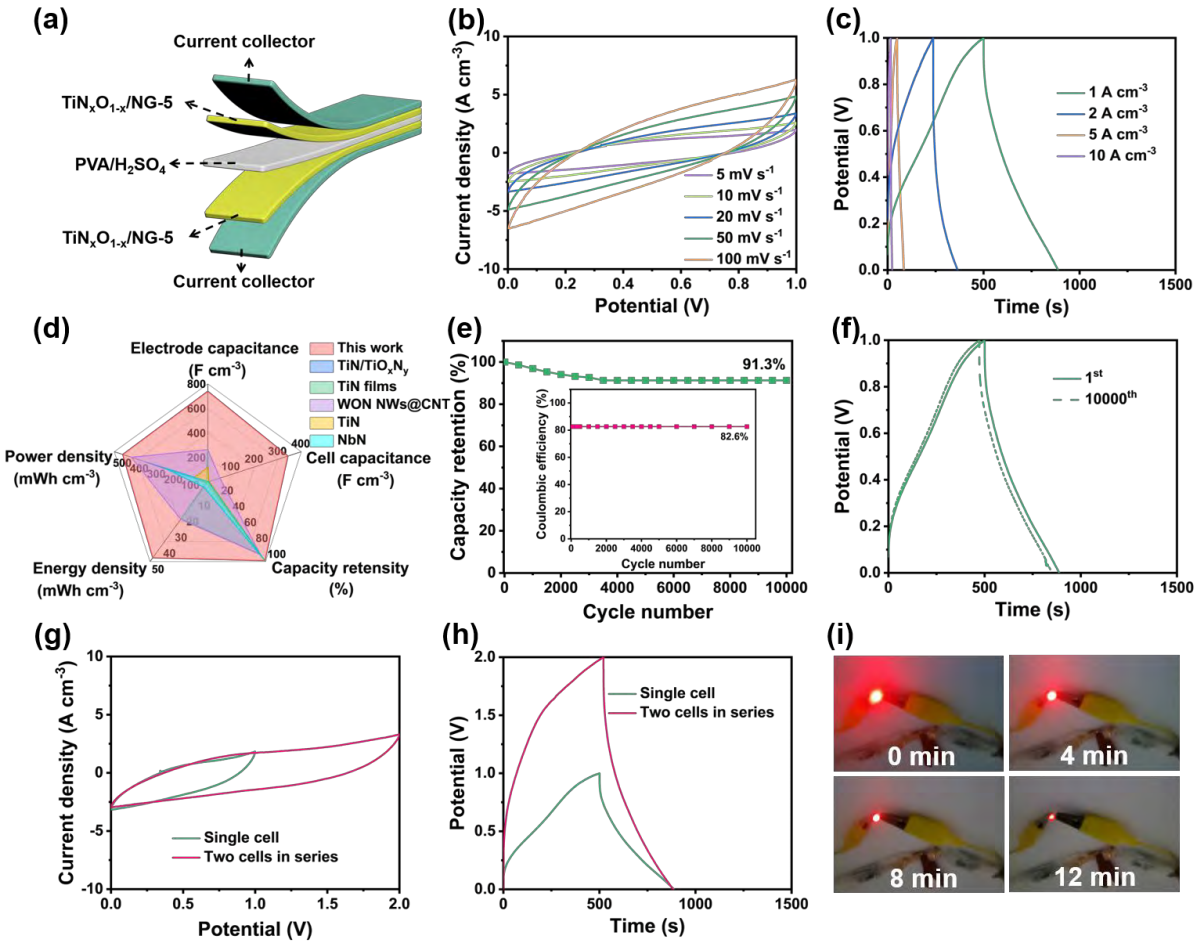

Fig. S29. (a) Schematic diagram of the symmetrical TiN_xO_{1-x}/NG-5//TiN_xO_{1-x}/NG-5 all-solid-state supercapacitor; (b) CV curves of the TiN_xO_{1-x}/NG-5-based device at different scanning rates; (c) GCD curves of the TiN_xO_{1-x}/NG-5-based device at different current densities; (d) Radar map comparing the performance of the TiN_xO_{1-x}/NG-5 electrode with other references; (e) Stability of the TiN_xO_{1-x}/NG-5-based device at a current density of 1 A cm^{-3} for 10,000 cycles, the inset is the Coulombic efficiency of the device during cycling; (f) The GCD curves at the first and last cycles; (g) CV and (h) GCD curves of the single and two devices in series at a current density of 1 A cm^{-3}; (i) The digital picture of a red LED lit by two devices in series.

Table S1. Comparison of capacitive performances of the as-synthesized TiN_xO_{1-x}/NG with other previously reported nitride or oxynitride-based materials.

Electrode material	electrode capacitance	Cell capacitance	Cyclability test	Energy density @ Power density	Refs.
TiN_xO_{1-x}/NG	**739.2 F cm^{-3} at 1 A cm^{-3}**	**342.6 F cm^{-3} at 1 A cm^{-3}**	**91.3%, 10000 cycles**	**47.6 mWh cm^{-3} @ 500.0 mW cm^{-3}**	**This work**
TiN	164.5 F g^{-1} at 5 mV s^{-1}	12.67 F g^{-1} at 100 mV s^{-1}	102.2%, 20000 cycles	3.26 mWh cm^{-3} @ 78.3 mW cm^{-3}	[8]
TiN/TiO_xN_y	6.19 F cm^{-3} at 0.01 mA cm^{-3}	0.77 F cm^{-3} at 1 V s^{-1}	90%, 10000 cycles	0.7 mWh cm^{-3} @ 359 mW cm^{-3}	[9]
TiN films	276 F cm^{-3} at 2.93 A cm^{-3}	1.66 F cm^{-3} at 1.66 A cm^{-3}	91%, 10000 cycles	23 mWh cm^{-3} @ 7.4 mW cm^{-3}	[10]
TiN	120 F cm^{-3} at 0.83 A cm^{-3}	5.9 F cm^{-3} at 0.02 A cm^{-3}	99 %, 3000 cycles	0.53 mWh cm^{-3} @ 0.08 W cm^{-3}	[11]
GaON	625 mF cm^{-2} at 10 mA cm^{-2}	132 mF cm^{-2} at 10 mA cm^{-2}	100%, 20000 cycles	0.35 mWh cm^{-3} @ 8.3 mW cm^{-3}	[12]
VN	60 mF cm^{-2} at 5 mV s^{-1}	17.3 mF cm^{-2} at 0.3 mA cm^{-2}	91.2%, 15000 cycles	21.2 mWh cm^{-3} @ 2.0 mW cm^{-3}	[13]
WN–rGOF	16.29 F cm^{-3} at 0.05 A cm^{-3}	16.29 F cm^{-3} at 0.05 A cm^{-3}	84.7% 10 000 cycles	1.448 mW h cm^{-3} @ 901.6 mW cm^{-3}	[14]
WON NWs@CNT	265 F cm^{-3} at 0.08 A cm^{-3}	52 F cm^{-3} at 0.5 A cm^{-3}	91.5% 5000 cycles	23.4 mW h cm^{-3} @ 0.45 W cm^{-3}	[15]
NbN	347.73 mAh g^{-1} at 0.2 A g^{-1}	2597 mF cm^{-3} at 60 mA cm^{-3}	97.7% 10,000	3.25 mWh cm^{-3} @ 254.2 mW cm^{-3}	[16]

Table S2. The detailed elemental contents of C, N, O, and Ti in N-TiO_2/NG, TiN_xO_{1-x}/NG-3, TiN_xO_{1-x}/NG-5, and TiN_xO_{1-x}/NG-7 by XPS analysis.

Samples	C at.%	N at.%	O at.%	Ti at.%	N/O ratio
N-TiO_2/NG	34.72	**7.79**	**39.22%**	18.27	**0.2**
TiN_xO_{1-x}/NG-3	34.29	**15.62**	**26.03**	24.06	**0.6**
TiN_xO_{1-x}/NG-5	33.95	**21.67**	**20.89**	23.49	**1.0**
TiN_xO_{1-x}/NG-7	33.01	**23.57**	**19.60**	23.82	**1.2**

Table S3. Deconvolution results of Ti 2*p* XPS data for N-TiO_2/NG, TiN_xO_{1-x}/NG-3, TiN_xO_{1-x}/NG-5, and TiN_xO_{1-x}/NG-7.

Samples	Ti 2p species	Peak area	Species proportion
N-TiO_2/NG	Ti-O	59018	80.5%
	N-Ti-O	**10704**	**14.6%**
	Ti-N	3592	4.9%
TiN_xO_{1-x}/NG-3	Ti-O	43329	59.1%
	N-Ti-O	**19062**	**26.0%**
	Ti-N	10924	14.9%
TiN_xO_{1-x}/NG-5	Ti-O	27787	37.9%
	N-Ti-O	**28080**	**38.3%**
	Ti-N	17449	23.8%
TiN_xO_{1-x}/NG-7	Ti-O	18974	25.6%
	N-Ti-O	**17121**	**23.1%**
	Ti-N	38024	51.3%

Table S4. Deconvolution results of Ti 2*p* XPS data for TiN_xO_{1-x}/NG-5, and TiN_xO_{1-x}-5.

Samples	Ti 2*p* species	Peak position (eV)	Peak area	Species proportion
TiN_xO_{1-x}/NG-5	Ti-O	458.59	27787	37.9%
	N-Ti-O	456.91	28080	38.3%
	Ti-N	455.52	17449	23.8%
TiN_xO_{1-x}-5	Ti-O	458.58	29629	52.3%
	N-Ti-O	457.15	16528	29.2%
	Ti-N	455.73	10519	18.5%

References

[1] T. Sasaki, F. Kooli, M. Iida, Y. Michiue, S. Takenouchi, Y. Yajima, F. Izumi, B.C. Chakoumakos, M. Watanabe, A mixed alkali metal titanate with the lepidocrocite-like layered structure. preparation, crystal structure, protonic form, and acid-base intercalation properties, Chem. Mater. 10 (1998) 4123−4128. https://doi.org/10.1021/cm980535f.

[2] C. Wang, X.L. Li, H. Song, P.K. Chu, K.F. Huo, In-plane heterostructured MoN/MoC nanosheets with enhanced interfacial charge transfer for superior pseudocapacitive storage, Adv. Funct. Mater. 34 (2024) 2311040. https://doi.org/10.1002/adfm.202311040.

[3] G. Kresse, J. Furthm ller, Efficiency of ab-initio total energy calculations for metals and semiconductors using a plane-wave basis set, Comput. Mater. Sci. 6 (1996) 15−50. https://doi.org/10.1016/0927-0256(96)00008-0.

[4] G. Kresse, J. Furthm ller, Efficient iterative schemes for ab initio total-energy calculations using a plane-wave basis set, Phys. Rev. B 54 (1996) 11169. https://doi.org/10.1103/PhysRevB.54.11169.

[5] J.P. Perdew, K. Burke, M. Ernzerhof, Generalized gradient approximation made simple, Phys. Rev. Lett. 77 (1996) 3865. https://doi.org/10.1103/PhysRevLett.77.3865.

[6] G. Kresse, D. Joubert, From ultrasoft pseudopotentials to the projector augmented-wave method, Phys. Rev. B 59 (1999) 1758. https://doi.org/10.1103/PhysRevB.59.1758.

[7] P.E. Bl chl, Projector augmented-wave method, Phys. Rev. B 50 (1994) 17953. https://doi.org/10.1103/PhysRevB.50.17953.

[8] B. Yao, M.M. Li, J. Zhang, L. Zhang, Y. Song, W. Xiao, A. Cruz, Y.X. Tong, Y. Li, TiN paper for ultrafast-charging supercapacitors, Nano-Micro Lett. 12 (2020) 1−13. https://doi.org/10.1007/s40820-019-0340-7.

[9] N.N. Sun, J. Xu, Y.P. Su, P. Jiang, Y.Z. Zou, W.W. Liu, M.X. Wang, D.Y. Zhou, Energy storage performance of in-situ grown titanium nitride current collector/titanium oxynitride

laminated thin film electrodes, Chem. Eng. J. 474 (2023) 145603. https://doi.org/10.1016/j.cej.2023.145603.

[10] N.N. Sun, D.Y. Zhou, W.W. Liu, S.Y. Shi, Z.J. Tian, F. Liu, S.D. Li, J.J. Wang, F. Ali, Tailoring surface chemistry and morphology of titanium nitride electrode for on-chip supercapacitors, ACS Sustainable Chem. Eng. 8 (2020) 7869−7878. https://doi.org/10.1021/acssuschemeng.0c00977.

[11] P. Qin, X.X. Li, B. Gao, J.J. Fu, L. Xia, X.M. Zhang, K.F. Huo, W.L. Shen, P.K. Chu, Hierarchical TiN nanoparticles-assembled nanopillars for flexible supercapacitors with high volumetric capacitance, Nanoscale, 10 (2018) 8728−8734. https://doi.org/10.1039/c8nr01485j.

[12] J.Y. Wang, F.X. Zhang, Z. Xu, W. Hu, H.H. Jiang, L.B. Liu, L.G. Gai, Gallium oxynitride@carbon cloth with impressive electrochemical performance for supercapacitors, Chem. Eng. J. 411 (2021) 128481. https://doi.org/10.1016/j.cej.2021.128481.

[13] Z.Q. Wu, B.B. Yang, H. Li, H.Y. Tong, X. Wang, H. Li, C.D. Li, L.L. Zhu, R.H. Wei, L. Hu, C.H. Liang, X.B. Zhu, Y.P. Sun, Solution-processable hierarchical-porous vanadium nitride films on silicon substrates for highly efficient symmetric supercapacitors, J. Power Sources 507 (2021) 230269. https://doi.org/10.1016/j.jpowsour.2021.230269.

[14] A. Salman, S.P. Sasikala, I.H. Kim, J.T. Kim, G.S. Lee, J.G. Kim, S.O. Kim, Tungsten nitride-coated graphene fibers for high-performance wearable supercapacitors, Nanoscale 12 (2020) 20239-20249. https://doi.org/10.1039/D0NR06636B.

[15] X.Q. Cheng, Z.H. Pan, J. Yang, Y.T. Zhong, X.S. Wang, C.C. Ye, J.C. Zhuang, Q.M. Huang, Q.Y. cai, W.S. Li, Tungsten oxynitride nanowires as negative electrode for fiber-shaped supercapacitor, J. Power Sources 427 (2019) 243-249. https://doi.org/10.1016/j.jpowsour.2019.04.097.

[16] D. Mandal, J. Y. Jeong, B.S. Singu, S. Lee, W.J. Mun, H. Kim, Flexible all solid-state niobium nitride//activated carbon lithium-ion hybrid capacitor with high volumetric power and energy densities, J. Energy Storage 48 (2022) 104031. https://doi.org/10.1016/j.est.2022.104031.